

5-1-2024

# Characterizing the Molecular and Cellular Changes of Senescent Cells Induced by Diverse Stressors in 2D and 3D Microenvironments

Apoorva Chauhan

Follow this and additional works at: <https://digitalscholarship.unlv.edu/thesesdissertations>



Part of the [Biomechanical Engineering Commons](#), [Biomedical Commons](#), and the [Biomedical Devices and Instrumentation Commons](#)

---

## Repository Citation

Chauhan, Apoorva, "Characterizing the Molecular and Cellular Changes of Senescent Cells Induced by Diverse Stressors in 2D and 3D Microenvironments" (2024). *UNLV Theses, Dissertations, Professional Papers, and Capstones*. 4969.

<http://dx.doi.org/10.34917/37650791>

This Thesis is protected by copyright and/or related rights. It has been brought to you by Digital Scholarship@UNLV with permission from the rights-holder(s). You are free to use this Thesis in any way that is permitted by the copyright and related rights legislation that applies to your use. For other uses you need to obtain permission from the rights-holder(s) directly, unless additional rights are indicated by a Creative Commons license in the record and/or on the work itself.

This Thesis has been accepted for inclusion in UNLV Theses, Dissertations, Professional Papers, and Capstones by an authorized administrator of Digital Scholarship@UNLV. For more information, please contact [digitalscholarship@unlv.edu](mailto:digitalscholarship@unlv.edu).

CHARACTERIZING THE MOLECULAR AND CELLULAR CHANGES OF SENESCENT  
CELLS INDUCED BY DIVERSE STRESSORS IN  
2D AND 3D MICROENVIRONMENTS

By

Apoorva Chauhan

Bachelor of Science – Mechanical Engineering  
University of Nevada, Las Vegas  
2022

A thesis submitted in partial fulfillment  
of the requirements for the

Master of Science – Biomedical Engineering

The Graduate College

University of Nevada, Las Vegas  
May 2024



## Thesis Approval

The Graduate College  
The University of Nevada, Las Vegas

April 17, 2024

This thesis prepared by

Apoorva Chauhan

entitled

Characterizing the Molecular and Cellular Changes of Senescent Cells Induced by  
Diverse Stressors in 2D and 3D Microenvironments

is approved in partial fulfillment of the requirements for the degree of

Master of Science – Biomedical Engineering  
The Graduate College

Seungman Park, Ph.D.  
*Examination Committee Chair*

Mohamed Trabia, Ph.D.  
*Examination Committee Member*

Janet Dufek, Ph.D.  
*Examination Committee Member*

Chandrabali Bhattacharya, Ph.D.  
*Graduate College Faculty Representative*

Alyssa Crittenden, Ph.D.  
*Vice Provost for Graduate Education &  
Dean of the Graduate College*

## ABSTRACT

### Characterizing the Molecular and Cellular Changes of Senescent Cells Induced By Diverse Stressors In 2D and 3D Microenvironments

By: Apoorva Chauhan

Dr. Seungman Park, Advisory Committee Chair

Assistant Professor

University of Nevada, Las Vegas

Aging is a risk factor for myriad diseases and is often associated with the accumulation of senescent cells. Cellular senescence, a process of irreversible cell cycle arrest, is associated with various changes in cellular morphology and function. While senescence will occur naturally in a time-dependent manner, it can be prematurely induced by various extrinsic and intrinsic factors. Most senescence studies model cell behavior in two-dimensional (2D) microenvironments; however, these models are not physiologically relevant. In this study, the effects of naturally occurring reactive oxygen species (ROS) hydrogen peroxide ( $H_2O_2$ ) and commonly used chemotherapy drugs, doxorubicin and palbociclib, on cellular senescence are modeled and compared in 2D and 3D replicas of skin tissue using human foreskin fibroblasts (HFF). This study shows that senescence associated cellular changes are not only stressor-dependent, but also environment dependent.

## TABLE OF CONTENTS

ABSTRACT.....	iii
TABLE OF CONTENTS.....	iv
LIST OF FIGURES .....	vi
CHAPTER 1: INTRODUCTION.....	1
1.1    Aging, Senescence, and Senescent Phenotypes .....	1
1.2 Stress Induced Premature Senescence.....	3
1.2.1 Senescence Inducers .....	3
1.2.2 Oxidative Stress Induced Senescence.....	3
1.2.3 Drug Therapy Induced Senescence .....	4
1.3 Skin Tissue Senescence Modelling .....	4
1.4 Objective .....	6
CHAPTER 2: METHODS.....	7
2.1 Cell Culture .....	7
2.2 2D Experimental Model .....	7
2.3 3D Experimental Collagen Model.....	8
2.4 Senescence Modeling.....	9
2.5 Senescence Feature Observation .....	10
2.5.1 SA $\beta$ -Gal Assay.....	10
2.5.2 MTT Assay .....	10
2.5.3 F-Actin Phalloidin Staining .....	11

2.5.4 Nuclear DAPI Staining .....	11
2.5.5 Imaging .....	12
2.6 Data Extraction.....	12
2.7 Statistical Analysis .....	12
CHAPTER 3: RESULTS AND DISCUSSION .....	13
3.1 Results of Concentration Dependent Changes in Functional Properties of Cell and Nucleus .....	13
3.2 Discussion: Concentration Dependent Changes in Functional Properties of Nucleus and Cell .....	20
3.3 2D vs. 3D Microenvironment Results.....	25
3.4 2D vs. 3D Microenvironment Discussion.....	32
CHAPTER 4: CONCLUSION .....	35
REFERENCES .....	37
CURRICULUM VITAE .....	46

## LIST OF FIGURES

Figure 1: Collagen gel casting protocol. ....	9
Figure 2: Experimental protocol and timeline. ....	10
Figure 3: Bright field and immunofluorescence images for H <sub>2</sub> O <sub>2</sub> treatment.....	13
Figure 4: Fluorescence intensity after treatment with H <sub>2</sub> O <sub>2</sub> . ....	14
Figure 5: Morphological properties of the nucleus and cell body after treatment with H <sub>2</sub> O <sub>2</sub> .....	15
Figure 6: Bright field and immunofluorescence images for Dox treatment .....	15
Figure 7: Fluorescence intensity after treatment with Dox.....	16
Figure 8: Morphological properties of the nucleus and cell body after treatment with Dox.....	17
Figure 9: Bright field and immunofluorescence images for Pal treatment .....	18
Figure 10: Fluorescence intensity after treatment with Pal .....	18
Figure 11: Morphological properties of the nucleus and cell body after treatment with Pal.....	19
Figure 12: MTT assay results for HFFs treated with each stressor.....	20
Figure 13: Bright field and immunofluorescence images for HFFs in collagen matrix. ....	25
Figure 14: Fluorescence images and quantification of nuclear morphological properties for optimized concentrations in 2D and 3D microenvironments. ....	27
Figure 15: Fluorescence images and quantification of cellular morphological properties for optimized concentrations in 2D and 3D microenvironments .....	29
Figure 16: Fluorescence images of SA β-Gal activity and quantification for 2D and 3D.....	30
Figure 17: Fluorescence images of phalloidin activity and quantification for 2D and 3D.....	31
Figure 18: Fluorescence images of DAPI activity and quantification for 2D and 3D.....	31

## CHAPTER 1

### INTRODUCTION

#### 1.1 Aging, Senescence, and Senescent Phenotypes

Aging is a pivotal risk factor for many diseases, including cardiovascular diseases, Alzheimer's disease, and cancer. It is characterized by the gradual deterioration of physiological functions within cells, tissues, and the entire organism (Phillip et al., 2015). A hallmark of aging is cellular senescence, or a state of permanent cell cycle arrest. In a senescent state, cells will no longer undergo mitosis; however, the cells remain metabolically active and will not undergo apoptosis (Muñoz-Espín & Serrano, 2014). Senescent cells exhibit a variety of different phenotypes as compared to healthy cells, including changes in morphology, cell and organelle function, and the secretion of materials known as senescence associated secretory phenotypes (SASPs) (Muñoz-Espín & Serrano, 2014).

Senescence can be caused by a variety of factors. Natural aging, or replicative senescence, is the shortening of DNA telomeres due to repeated proliferation, preventing cells from splitting further (Kuilman et al., 2010). This telomere attrition triggers a DNA damage response (DDR) that results in the formation of heterochromatin aggregates within the nucleus. These foci have become markers of senescence, dubbed senescence associated heterochromatin foci (SAHF) (Zeng et al., 2018). Along with the formation of SAHF, the p53 pathway, p16 kinase, and retinoblastoma (Rb) protein are all upregulated (Kuilman et al., 2010). The p53 pathway is a tumor suppressor that regulates cell cycle progression, leading to the arrest seen in senescence, as well as DNA damage repair and cell death in response to dysfunctional cell activity (Lahalle et al., 2021). Similarly, the p16 kinase and Rb protein act in the same pathway as tumor suppressors. Cyclin dependent kinase



(CDK) 4/6 normally acts to prevent the phosphorylation of Rb; p16 is a CDK inhibitor, and when activated leads to the overexpression of Rb (Narita et al., 2003).

Along with indicators of halted cell cycle, a widely used biomarker for senescence is the presence of senescence associated  $\beta$ -galactosidase (SA  $\beta$ -Gal).  $\beta$ -Gal is the enzyme that catalyzes the breakdown of lactose and is commonly found in cells at a pH of 4.0 (Saqib et al., 2017). Due to the altered gene expression common in senescence,  $\beta$ -Gal will accumulate because of the overexpression of its gene encoder, GLB1, and be detectable at the senescent pH of 6.0 (Valieva et al., 2022). However, SA  $\beta$ -Gal is also overexpressed during autophagy, the turnover process for damaged or unneeded cellular components and proteins which is regulated through lysosomal activity (de Mera-Rodríguez et al., 2021; Young et al., 2009). As such, SASP expression and morphological changes must also be assessed to determine senescence.

SASPs regulate and maintain senescence, while also signaling to nearby cells to enter senescence. Interleukins and chemokines, such as IL-6 and IL-8, are inflammatory factors upregulated in senescence; matrix metalloproteinases (MMPs) are also upregulated and are involved in the breakdown of extracellular matrix (ECM) components such as collagen; an insoluble factor often upregulated, called fibronectin, alters cell growth, adhesion, survival, and migration (Coppé et al., 2010). Along with these biochemical changes, senescent cells depict a unique morphology. Senescent cells are larger, flatter, and more misshapen as compared to healthy cells (Huang et al., 2022). Additionally, the nuclei of these cells are often larger and misshapen as well, possibly due to the downregulation of Lamin B1, the protein that forms the nuclear envelope; in some cases, cells will even have multiple nuclei (Freund et al., 2012). These morphological changes are well documented, though often only qualitatively measured.

## 1.2 Stress Induced Premature Senescence

### 1.2.1 Senescence Inducers

While these factors are generally seen in senescent cells, the consistency of these SASPs and morphology changes can differ depending on cell type or senescence inducer. Cellular senescence can also be prematurely induced, referred to as stress induced premature senescence (SIPS) (Toussaint et al., 2002). Exposure to UV radiation leads to senescence inducing damage and is referred to as photoaging; fluctuations in hydrostatic pressure, as seen in blood vessels or cases of osteoarthritis, cell function is altered; microgravity and vacuum environments induce cellular and tissue alterations through abnormal mechanical stresses (Fitsiou et al., 2021; Garbacki et al., 2023; Tworkoski et al., 2018). However, some of the most common and most studied causes of premature senescence are oxidative stress and cancer drugs. Oxidative stress is caused by the accumulation of reactive oxygen species (ROS) which can induce DNA damage and alter metabolic activity (Toussaint et al., 2000). Where senescence is an unintended side effect of other stress inducing factors, cancer drugs utilize senescence as a method to prevent tumors from progressing (Ewald et al., 2010). Due to the prevalence in exposure to these stressors, ROS and cancer therapies are highly relevant aging causing factors, and the ones chosen to investigate further.

### 1.2.2 Oxidative Stress Induced Senescence

ROS are byproducts of various endogenous processes, namely from the mitochondrial activity in ATP production (Snezhkina et al., 2019). The superoxide radical,  $O_2^{\bullet-}$ , is converted to hydrogen peroxide ( $H_2O_2$ ), a less toxic but still harmful ROS. ROS induced DNA damage results in the activation of the p53 tumor suppressant pathway, similar to replicative senescence, and as a result induces senescence or even cell death if severe enough (Duan et al., 2005).

### 1.2.3 Drug Therapy Induced Senescence

In 2023, nearly 2 million Americans were diagnosed with cancer, with breast cancer having the highest prevalence of 31% of all female cases, followed by prostate cancer which is 29% of all male cases, and lung cancer which is the second highest for both sexes (Siegel et al., 2024). To prevent tumor metastasis, cancer therapies often target the cell's replicative abilities, leading to either apoptosis or senescence (Gordon & Nelson, 2012). Doxorubicin (Dox) is the most commonly used anthracycline, which blocks the production of the enzyme topoisomerase 2, in turn inhibiting cell growth and division (Xiao et al., 2023). Its cytotoxicity often also induces ROS and in turn causes DNA damage that triggers a senescence response. Dox is used to treat many different cancers, including breast and lung (Johnson-Arbor & Dubey, 2024). Palbociclib (Pal) is a CDK4/6 inhibitor used in breast cancer treatment. Similar to p16, Pal prevents the phosphorylation of Rb, leading to cell cycle arrest, as well as increased levels of ROS, DNA damage, and apoptosis (Wagner & Gil, 2020).

### 1.3 Skin Tissue Senescence Modelling

When studying disease progression, and especially the effects of aging on disease, the skin is a vital organ to investigate. Skin acts as a protective barrier, but the accumulation of senescent cells can weaken its ability to protect from extrinsic and intrinsic risk factors (Csekes & Račková, 2021; Low et al., 2021a). As a result, the study of skin tissue has become central to aging research, with much research being conducted using fibroblasts, the primary skin cell in the dermis. In this study, human foreskin fibroblasts (HFF) are used to replicate skin tissue behavior.

Most studies of senescence happen in two-dimensional (2D) cell cultures. In fact, all the literature addressed above is taken from 2D studies. While valuable, the studies show that there

are marked differences in cell function in 2D models as compared to a more physiologically relevant three-dimensional (3D) model. 3D modeling, also referred to as organotypic culture, consists of tissue explants taken from donors, organoids, and manufactured 3D structures and scaffolds (Milligan et al., 2020). Animal models, such as aged mice models, have lost popularity due to lack of translatability to human senescence progression, as well as dispute over when the mice are considered aged (Low et al., 2021b). Tissue explants, be it cultures derived from a harvested organ or specific slices of tissue, provide the most ideal model, as they are true to life. However, accessibility and replicability of these models can be difficult. As a result, the fabrication of 3D models, through organoids and scaffolds/structures, has become a vital field in senescence research.

Organoids are a form of 3D culture created primarily from embryonic stem cells (ESCs) and induced pluripotent stem cells (iPSCs). These stem cells will spontaneously aggregate and self-organize to form organ-like structures that replicate the form and function of the true organ (Milligan et al., 2020; Torrens-Mas et al., 2021). These models have the benefit of being patient-specific, as well as being the best replicates of true organ behavior. Organoids are popular in the field of neurodegenerative and aging related disease modeling (Torrens-Mas et al., 2021). However, as organoids are created from stem cells, which are juvenile in nature, they often lack the epigenetic markers of aging (Torrens-Mas et al., 2021). Additionally, organoid formation can be time consuming and expensive, reducing accessibility and replicability. 3D structures and scaffolding provide an attractive alternative to organoids in terms of manufacturing ability, though this may come at the cost of tissue complexity. These types of cultures can include cell suspensions in a polymer matrix, 3D bioprinted models, decellularized tissues, and organ-on-a-chip models

(Milligan et al., 2020). These methods use organic materials to provide a scaffold that mimics the ECM and can be modified to be as simple or complex as desired.

#### 1.4 Objective

In this study we examine the differences in morphology and protein expression of HFFs in 2D and 3D environments when prematurely aged with H<sub>2</sub>O<sub>2</sub>, doxorubicin, and palbociclib. The 2D environment is a simple cell culture, which consists of a monolayer of cells grown in a 24 well-plate, and the 3D environment is modeled by a rat tail collagen polymer matrix. By comparing the results, we aim to determine how senescence inducing stressors affect the cell environment and create more physiologically relevant skin tissue models that can be used for disease modeling and therapy development.

## CHAPTER 2

### METHODS

#### 2.1 Cell Culture

Human foreskin fibroblast HFF-1 (ATCC SCRC-1041) cells obtained from the American Type Culture Collection (Rockville, MD, USA) were cultured in Dulbecco's Modified Eagle Medium (DMEM) (Gibco, Waltham, MA, USA) containing 10% fetal bovine serum (FBS) (Cytiva, Marlborough, MA, USA) and 1% Penicillin-Streptomycin (P/S) (Gibco, Waltham, MA, USA). Cell culture media was replaced with fresh media every three days, and cells were subcultured and used for experiments when confluency was 70% or higher. Cells were incubated at 37 °C with 5% CO<sub>2</sub> in 100 mm X 20 mm mm Petri dishes. Cells used in the 2D experiments were between 15-25 passages, and cells used in 3D experiments were between 10-20 passages.

#### 2.2 2D Experimental Model

When cell confluency reached 70% or higher, cells were ready for seeding into experimental dishes. After discarding media, cells were detached from Petri dish surface by adding 2 mL of 0.25% trypsin-EDTA (Gibco, Waltham, MA, USA) and incubating in the dish for 5 minutes. Cells were washed with 5 mL of phosphate buffer saline (PBS) (Gibco, Waltham, MA, USA) and deposited into test tube for centrifuging at 2000 RPM for 5 minutes. After disposing of supernatant, the cell pellet was gently dispersed in the remaining 1 mL of PBS solution, and 6 mL of fresh media was added. In a 1mL vial, 50 µL of cell suspension was added to 100 µL of PBS and 50 µL of 0.4% trypan blue (Gibco, Waltham, MA, USA). Cell counting was conducted using standard procedure for Neubauer Improved Hemacytometer (LW Scientific, Lawrenceville, GA, USA). Cells were seeded into 18 of the 24 wells of a 24-well plate at a density of 100,000 cells

per well for three wells of control and each of the five experimental concentrations. 300  $\mu$ L of fresh media was added to each well. Cells were given 24 hours to attach to the well surface before experimentation.

### 2.3 3D Experimental Collagen Model

For 3D collagen models, the same cell counting procedure was followed as in 2D experimental setup. A cell pellet of 400,000 cells was prepared. 10X MEM (Gibco, Waltham, MA, USA) and 0.1 M HEPES (Gibco, Waltham, MA, USA) were warmed in a water bath to 37 °C. L-Glutamine (Gibco, Waltham, MA, USA), FBS, and P/S were thawed in the water bath. Sterile 1.0 M NaOH and deionized H<sub>2</sub>O were kept on ice inside the biosafety cabinet. To a test tube sitting on ice, 10X MEM, NaOH, HEPES, P/S, L-Glutamine, FBS, and dH<sub>2</sub>O were combined and mixed with the cell pellet. 8.08 mg/mL type 1 rat tail collagen (Discovery Labware Inc., Bedford, MA, USA) was added to the solution. 200  $\mu$ L of the cellated collagen solution were added to each well for a total of 12 wells: 3 for control and 3 each for the optimal concentration of each stressor. Models were given two days for cells to attach and grow within the collagen scaffold before experimentation. Figure 1 shows the collagen gel casting protocol.

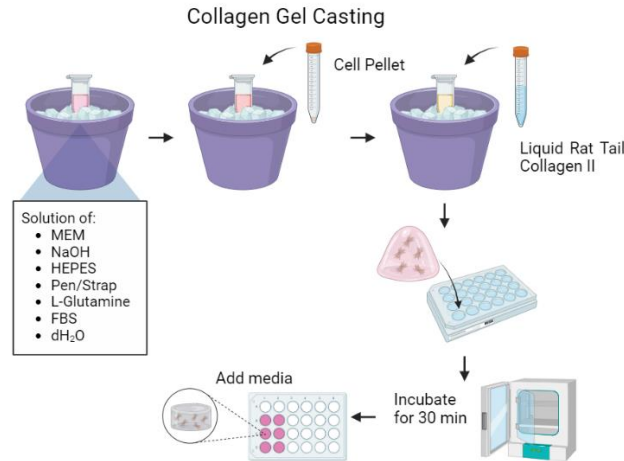


Figure 1: Collagen gel casting protocol.

## 2.4 Senescence Modeling

To create the H<sub>2</sub>O<sub>2</sub> diluted concentrations, 9.8 M H<sub>2</sub>O<sub>2</sub> was combined with the treated DMEM cell culture medium to make the following concentrations: 25  $\mu$ M, 50  $\mu$ M, 100  $\mu$ M, 150  $\mu$ M, and 200  $\mu$ M. Cells were incubated with H<sub>2</sub>O<sub>2</sub> for 1 hour. After 1 hour, H<sub>2</sub>O<sub>2</sub> solutions were discarded, and cells were washed with PBS. Fresh cell culture media was deposited, and cells were incubated for 23 hours. This protocol was developed based on the findings of Gerasymchuk et al. who found this method was sufficient to observe senescence phenotypes in cells when exposed to H<sub>2</sub>O<sub>2</sub> (Gerasymchuk et al., 2022). 1 mM Dox was combined with treated DMEM to create the following concentrations: 25 nM, 50 nM, 100 nM, 200 nM, and 400 nM. Cells were incubated with Dox for 48 hours. 2 mM Pal was combined with treated DMEM to create the following concentrations: 2.5  $\mu$ M, 5  $\mu$ M, 10  $\mu$ M, 20  $\mu$ M, and 40  $\mu$ M. Cells were incubated with Pal for 24 hours. Following treatment, senescence features were observed through fluorescent microscopy, SA  $\beta$ -Gal assay, MTT cell viability assay, f-actin phalloidin staining, and nuclear DAPI staining. Figure 2 outlines the experimental procedure and timeline for both 2D and 3D models. Three trials of each 2D and 3D model were conducted.



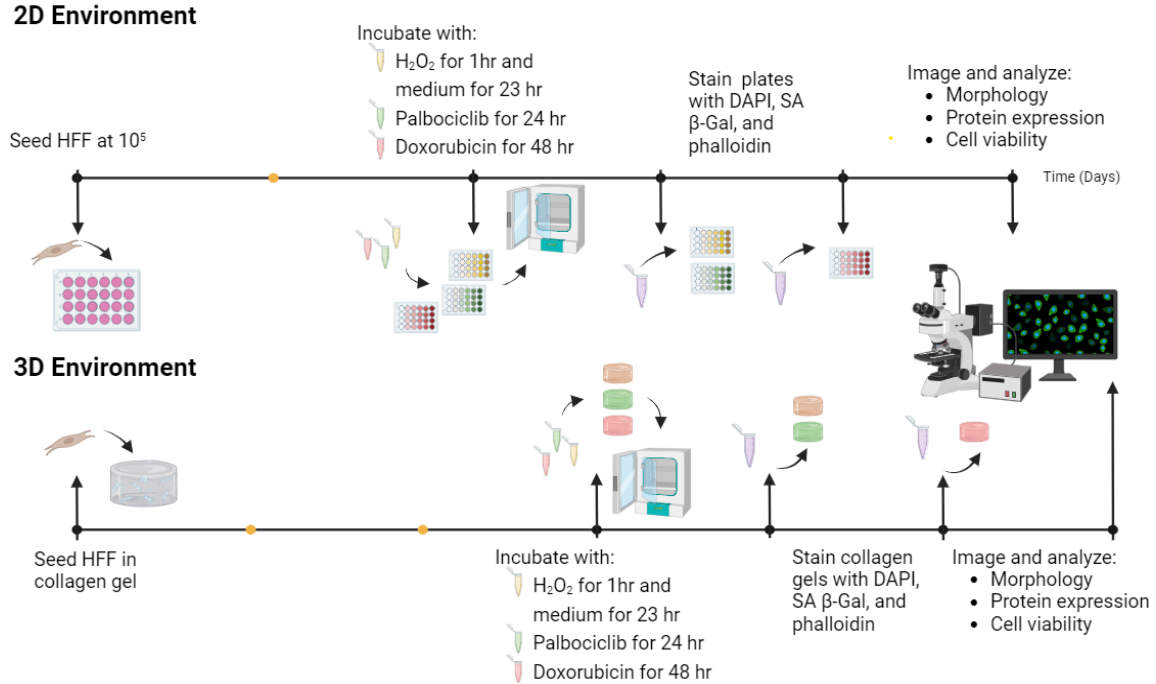


Figure 2: Experimental protocol and timeline.

## 2.5 Senescence Feature Observation

After treatment, models were fixed with 4% paraformaldehyde (TissuePro Technology, Gainesville, FL, USA). After fixing, cells are stored with PBS in a 4 °C refrigerator.

### 2.5.1 SA $\beta$ -Gal Assay

The Invitrogen CellEvent Senescence Green Detection Kit (Invitrogen, Waltham, MA, USA) was used to conduct the SA  $\beta$ -Gal staining. After the 2D and 3D models were fixed, 200  $\mu$ L of 1% Bovine Serum Albumin (BSA) (Sigma-Aldrich, St. Louis, MO, USA) was added to permeabilize the cells. After removing BSA and washing with PBS, 150  $\mu$ L of the SA  $\beta$ -Gal dye dilution was added to each well. The dilution was formulated following the protocol included with the kit. The well plates were covered in aluminum foil and incubated for 2 hours at 37 °C without  $CO_2$ . After 2 hours, SA  $\beta$ -Gal solution was removed and models are washed and stored with PBS.

### 2.5.2 MTT Assay

A confluent dish of HFFs was harvested by trypsinization and 100,000 cells were deposited to each well of a 96-well plate. After 16 hours of incubation at 37 °C with 5% CO<sub>2</sub> to allow cells to attach to plate, H<sub>2</sub>O<sub>2</sub>, Dox, or Pal treatment was conducted as described above. The media after the treatment period was replaced with the MTT reagent (Invitrogen, Waltham, MA, USA) and the plate was incubated for 4 hours. Post incubation, the media was removed and 100 µL of DMSO was added to the wells to solubilize formazan crystals to develop color. The readings were recorded at 550 nm using a UV plate reader (Promega GloMax Explorer Multimode Microplate Reader, USA). The relative cell viabilities were calculated by comparing the absorbance reading from test samples to the positive control [(abs. sample/abs. positive control) X 100]. Data are presented as average ± SD for three trials.

#### 2.5.3 F-Actin Phalloidin Staining

Models were permeabilized with 200 µL of 0.1% triton X for 5 minutes at room temperature. After discarding and washing with PBS, models were treated with 200 µL of 1% BSA for 5 minutes. After discarding and washing with PBS, Phalloidin 594 (Abcam, Cambridge, UK) dye was diluted at a ratio of 1 µL into 1 mL of 1% BSA and 150 µL was added into each well. The plates were covered in aluminum foil and incubated for 30 minutes for 2D or 1 hour for 3D at 37 °C without CO<sub>2</sub>. After incubation, phalloidin solution is discarded and models are washed and stored with PBS.

#### 2.5.4 Nuclear DAPI Staining

Invitrogen DAPI (4', t-diamidino-2-phenylindole, dihydrochloride) (Invitrogen, Waltham, MA, USA) was used to create DAPI staining solutions at a ratio of 0.1 µL of DAPI with 1 mL PBS. 150 µL of DAPI solution was added to each model, and well plates were covered in aluminum

foil and left at room temperature for 8 to 10 minutes. After, DAPI solution was discarded, and models washed with PBS.

### 2.5.5 Imaging

Well plates were imaged using the EVOS XL Core Imaging System (Invitrogen, Waltham, MA, USA) at 20X objective. Bright field images were taken to confirm the presence of cells. The green fluorescent protein (GFP) filter was used to image SA  $\beta$ -Gal expression; the red fluorescent protein (RFP) filter was used to image f-actin expression; and the DAPI filter was used to image the nuclear staining.

### 2.6 Data Extraction

ImageJ (NIH, MD, USA) software was used for data extraction. Images taken during microscopy were opened in the software and the image properties were adjusted to convert pixels into  $\mu\text{m}$ . Using the drawing tools, cells and nuclei were outlined and measured. From the GFP images, the average pixel intensity of each cell was recorded to measure SA  $\beta$ -Gal expression. From the RFP images, the cell body perimeter, area, and f-actin expression were measured. From the DAPI images, the nucleus perimeter, area, and staining intensity were measured. From each individual trial, 90 samples were measured. Each trial was repeated three times, for a total sample size of 270 for each experimental group.

### 2.7 Statistical Analysis

Excel was used to conduct ANOVA and t-test analyses to determine if there were any statistically significant changes between the measured values. Graphs were created using Prism. Data are presented as average  $\pm$  SEM for  $n = 270$ .

## CHAPTER 3

### RESULTS AND DISCUSSION

#### 3.1 Results of Concentration Dependent Changes in Functional Properties of Cell and Nucleus

To determine the optimal concentration of each stressor that would induce senescence without causing excessive cell death, five concentrations of each stressor was tested in a 2D environment. Figure 3 shows the bright field, DAPI, SA  $\beta$ -Gal, and phalloidin images for HFFs treated with  $H_2O_2$ . Along with the expected increase in SA  $\beta$ -Gal intensity, phalloidin also visibly increased in intensity. This observation led to quantifying the change in intensity for DAPI and phalloidin as well.

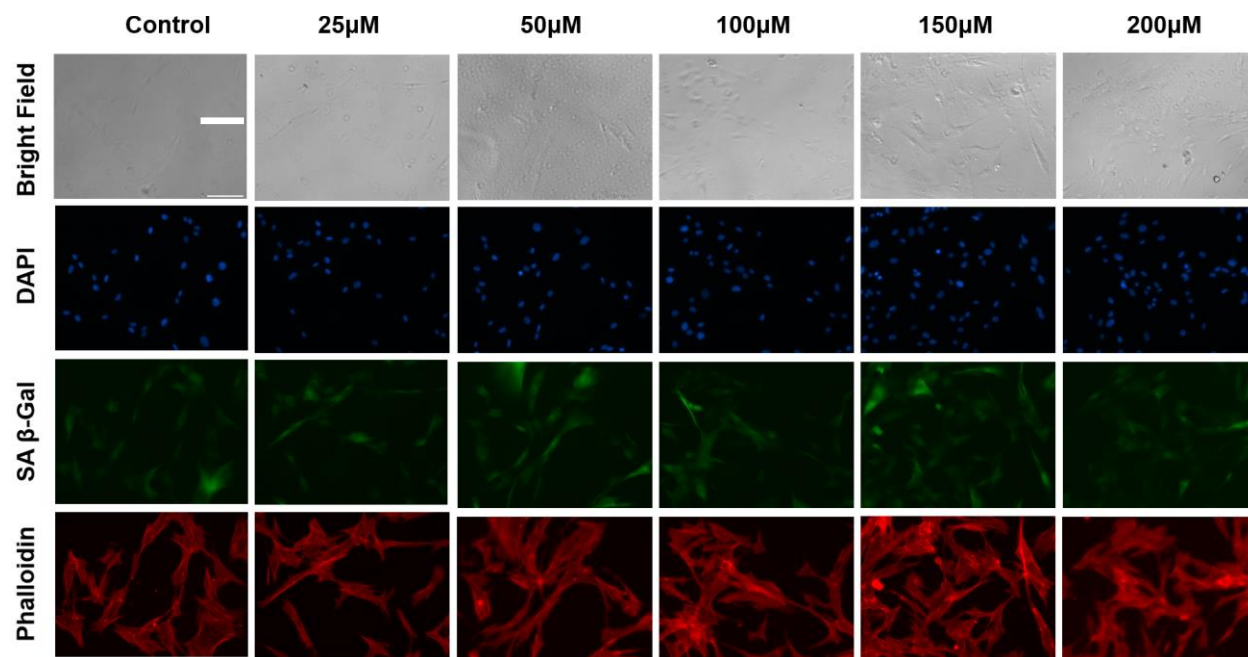


Figure 3: Bright field and immunofluorescence images of DAPI, SA- $\beta$ -gal, and phalloidin for  $H_2O_2$  treatment. Scale bar 200  $\mu$ m.

Figure 4 illustrates the relative fluorescence intensity of each staining reagent with different concentrations of  $H_2O_2$ . The overall trend observed was an increase in intensity levels of DAPI,

SA  $\beta$ -Gal, and phalloidin in cells treated with  $H_2O_2$  at or above 50  $\mu M$  of  $H_2O_2$ . Notably, at 50  $\mu M$  and 100  $\mu M$ , statistically significant increases in the intensity of DAPI, SA  $\beta$ -Gal, and phalloidin were observed.

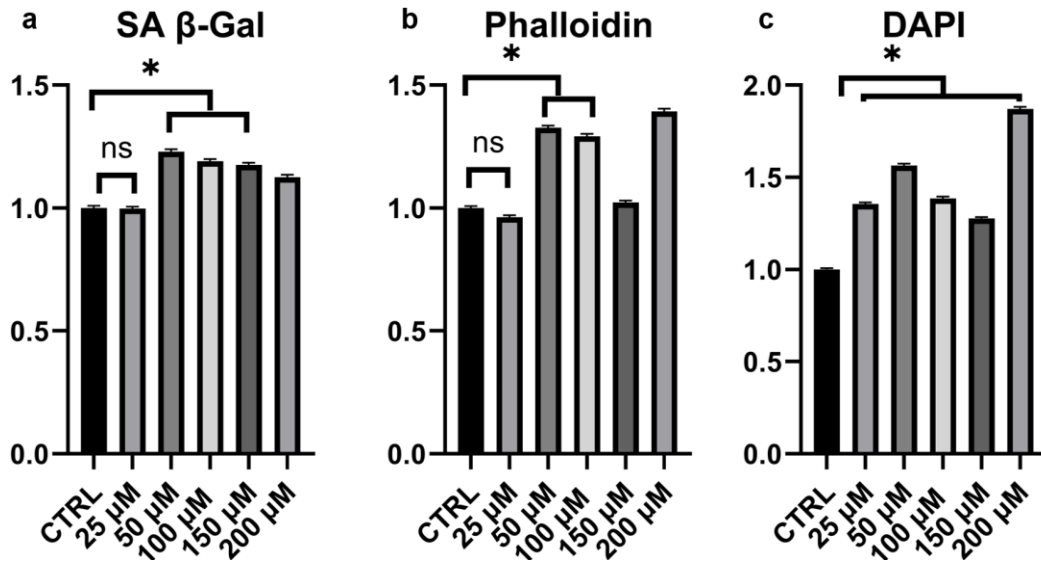


Figure 4: Fluorescence intensity of (a) SA  $\beta$ -Gal, (b) phalloidin, and (c) DAPI after treatment with  $H_2O_2$ .  $N = 270$ , \*  $p \leq 0.05$ . Data presented as mean  $\pm$  SEM.

Figure 5 shows the morphological properties for the nucleus and cell body of HFFs treated with  $H_2O_2$ . For the nucleus, both perimeter and area exhibited significantly higher values across a concentration range of 100 – 200  $\mu M$  compared to those observed in the control group. However, there was almost no discernible difference in shape index between the control group and the  $H_2O_2$ -treated groups, except for 200  $\mu M$  displaying the lower shape index. For the cell body, a significant change in area was observed at or above 50  $\mu M$  compared to the control group, while both the perimeter and shape index of the cell body remained constant.

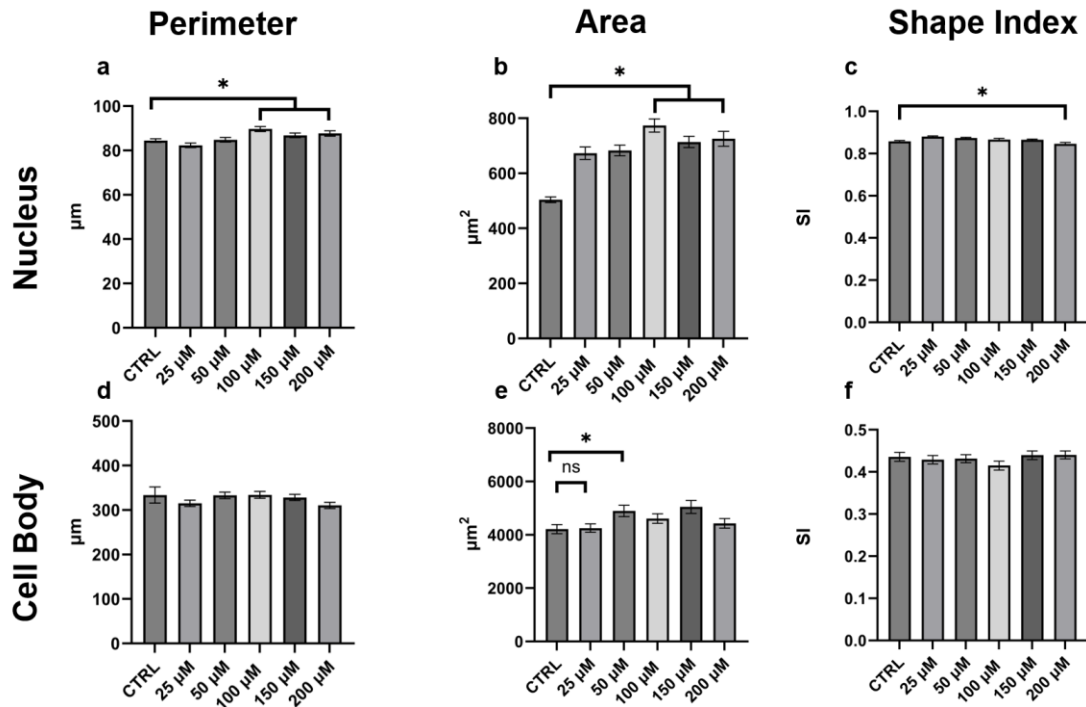


Figure 5: Morphological properties of the nucleus and cell body after treatment with H<sub>2</sub>O<sub>2</sub>. N = 270, \*  $p \leq 0.05$ . Data presented as mean  $\pm$  SEM.

Figure 6 shows the bright field, DAPI, SA  $\beta$ -Gal, and phalloidin images for HFFs treated with Dox.

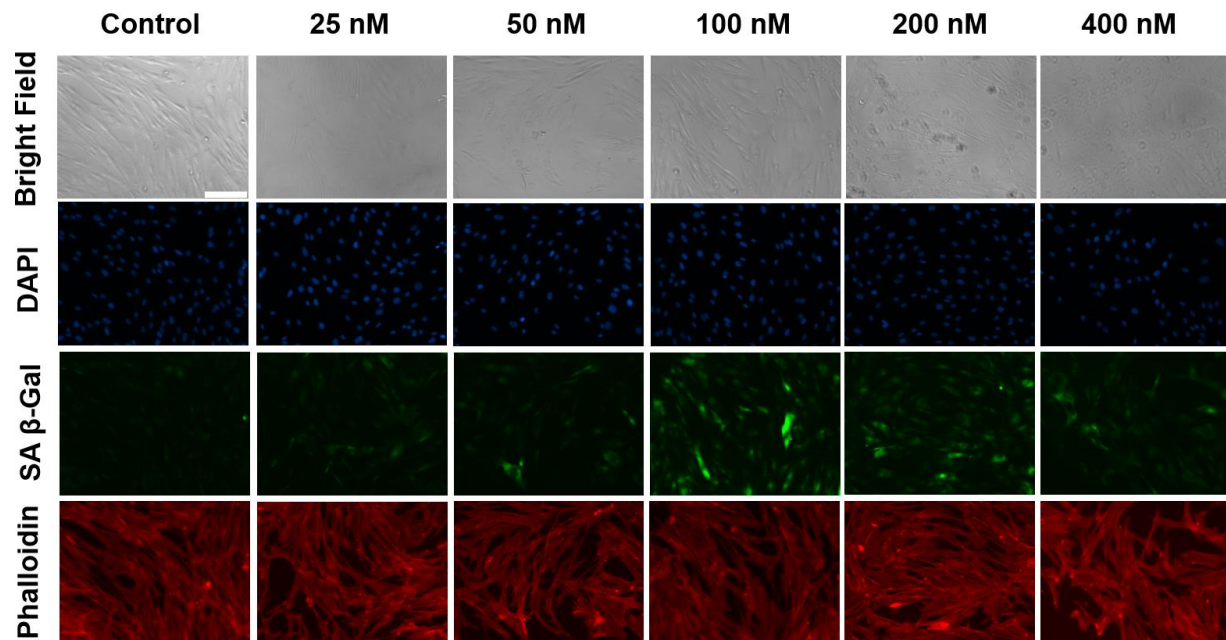


Figure 6: Bright field and immunofluorescence images for Dox treatment. Scale bar 200  $\mu$ m.

Figure 7 summarizes the relative fluorescence intensity values depending on the applied concentration. SA  $\beta$ -Gal exhibited a notable increase in its expression at and above 100 nM, whereas phalloidin and DAPI demonstrated significant increases at all concentrations. Combining these findings with cell viability assessed through the MTT assay, we concluded that 100 nM represents the optimal concentration for inducing cellular senescence while maintaining cell viability.

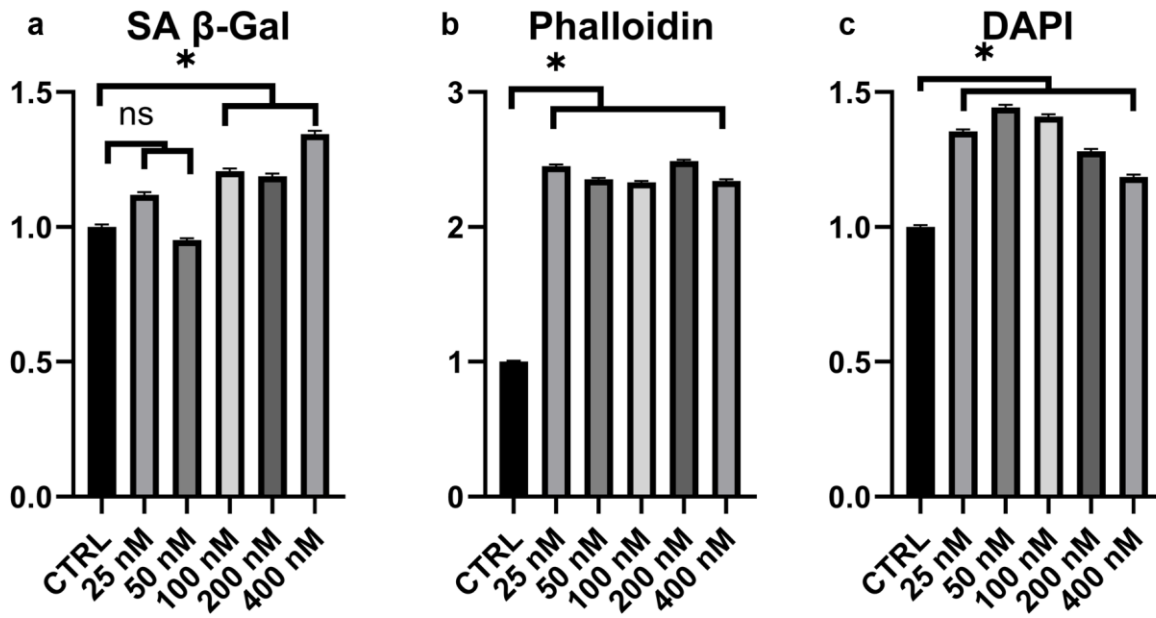


Figure 7: Fluorescence intensity of DAPI, SA  $\beta$ -Gal, and phalloidin after treatment with Dox. N = 270, \*  $p \leq 0.05$ . Data presented as mean  $\pm$  SEM.

Based on the fluorescence images, several morphological properties of the cellular nucleus and body were quantified, as shown in Figure 8. For the nucleus, both perimeter and area were found to be higher at dox concentrations at or above 50 nM, compared to the control group. Regarding the cell body, the perimeter significantly increased across the dox concentration range, while the area showed increments only at 50 nM and 400 nM. The shape index of the nucleus was lower at the 100 nM treatment compared to the control group, showing a statistically significant

difference. However, the shape index of the cell body treated with dox was consistently lower than that of the control group, regardless of concentration. Most importantly, we observed statistically significant changes in the morphological properties of the cell nucleus and body at concentrations of 50 nM or 100 nM.

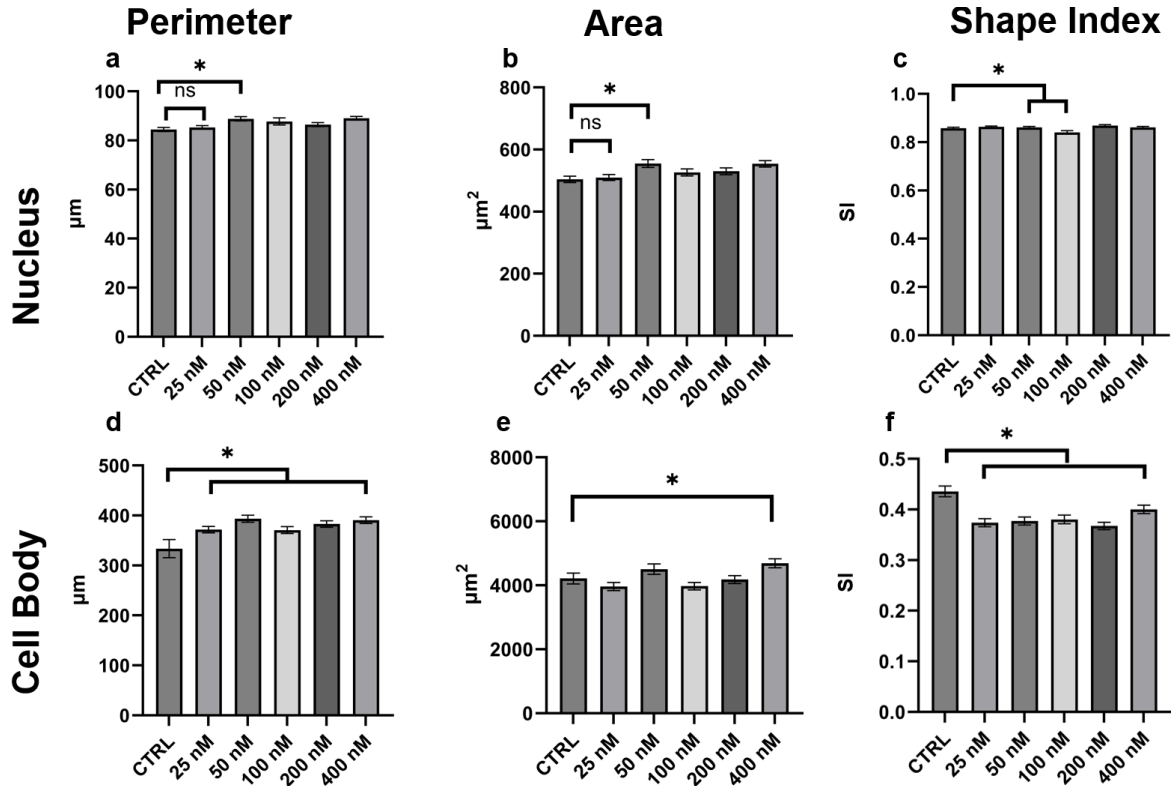


Figure 8: Morphological properties of the nucleus and cell body after treatment with Dox. N = 270, \*  $p \leq 0.05$ . Data presented as mean  $\pm$  SEM.

Figure 9 shows the bright field, DAPI, SA  $\beta$ -Gal, and phalloidin images for HFFs treated with Pal with concentrations ranging from 2.5  $\mu\text{M}$  to 40  $\mu\text{M}$ .



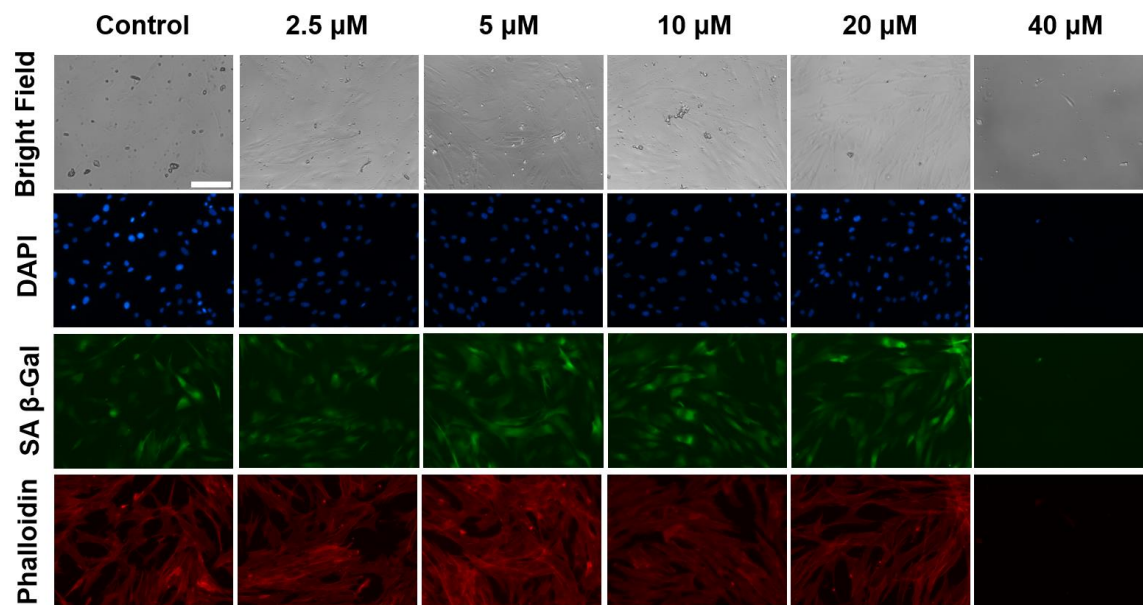


Figure 9: Bright field and immunofluorescence images for Pal treatment. Scale bar 200  $\mu\text{m}$ .

Figure 10 shows the relative fluorescence intensity values for the Pal treated cells. The overall trend in relative intensity changes after the addition of Pal reveals an elevation in intensities across concentrations for all fluorescence staining. Particularly noteworthy is that the concentration of 2.5  $\mu\text{M}$  was the only one displaying statistically significant increases in intensity.

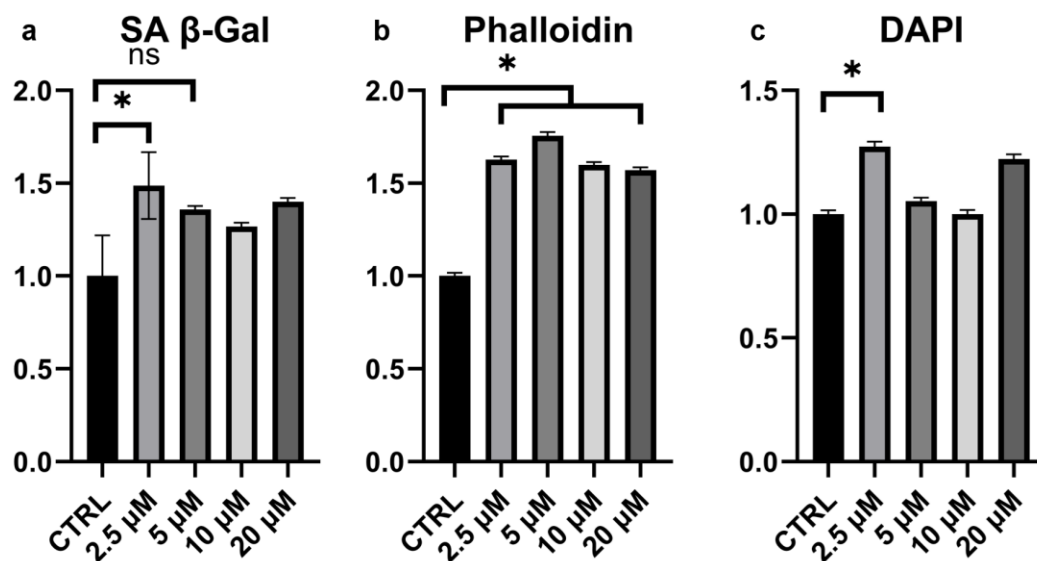


Figure 10: Fluorescence intensity of DAPI, SA  $\beta$ -Gal, and phalloidin after treatment with Pal. N = 270, \*  $p \leq 0.05$ . Data presented as mean  $\pm$  SEM.

Figure 11 shows the quantified results of morphological properties for HFFs after treatment with Pal with different concentrations. Results showed that both the perimeter and area of the cellular body and nucleus exhibit substantial elevation after Pal treatment, compared to those of the control group, displaying statistically significant difference. Notably, in the case of the nucleus, the shape index increased more compared to the control group, indicating that the cellular nucleus becomes more circular. However, in the cell body, the shape index decreased more compared to the control group, suggesting that the cellular nucleus becomes less circular.

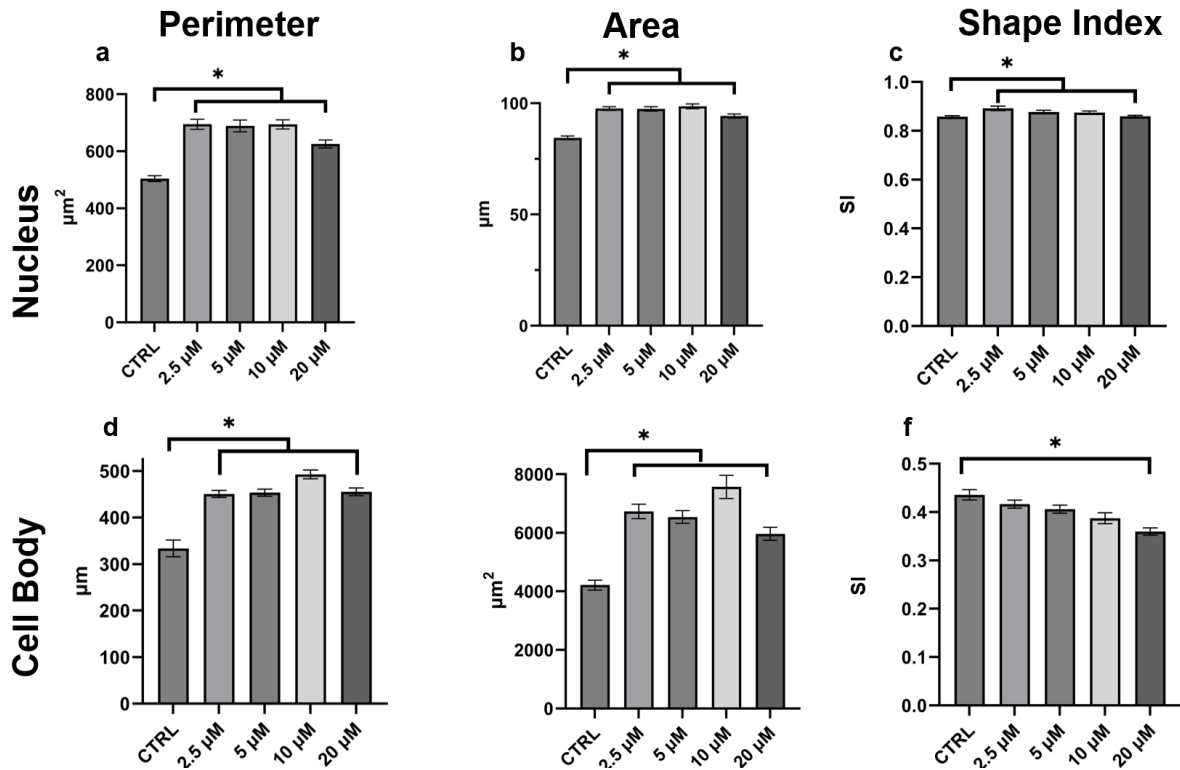


Figure 11: Morphological properties of the nucleus and cell body after treatment with Pal. N = 270, \*  $p \leq 0.05$ . Data presented as mean  $\pm$  SEM.

Figure 12 shows the results of the MTT assay conducted.  $H_2O_2$  treatment did not result in much cell death until 200  $\mu M$ , which reduced cell viability to about 80%. Dox and Pal treatment

saw greater reductions in cell viability at even the lowest dosages, with Dox at 100 nM maintaining cell viability of 80% and Pal at 2.5  $\mu$ M.

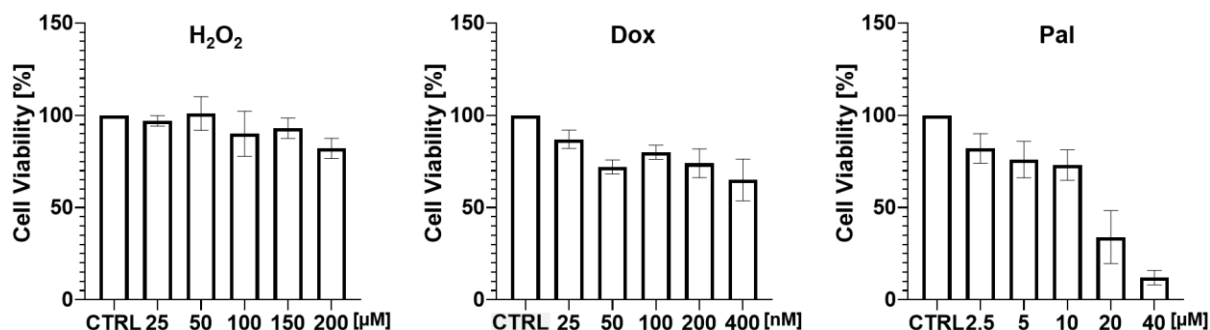


Figure 12: MTT assay results for HFFs treated with each stressor. N = 3. Data presented as mean  $\pm$  SEM.

### 3.2 Discussion: Concentration Dependent Changes in Functional Properties of Nucleus and Cell

Based on the aforementioned assays investigating the effects of concentrations on diverse functional properties, we identified the optimal concentrations for inducing cellular senescence as 100  $\mu$ M for  $H_2O_2$ , 100 nM for Dox, and 2.5  $\mu$ M for Pal. These concentrations were sufficient to induce statistically significant changes in cell and nucleus morphology, as well as changes in protein expression, without reducing cell viability below 80%. A documented marker of senescence is cell enlargement, which we measured through changes in the perimeter, area, and shape index; additionally, the nuclei also appeared enlarged, and cells may even have multiple nuclei (Schmitt & Melk, 2022). While the results did not always display a statistically significant difference, all three stressors tended to induce increases in the perimeter, area, or both for the cell body and the nucleus. The shape index was expected to decrease after treatment, as the cell shape became irregular and elongated after or during senescence. This was the case after treatment with Dox and Pal, however  $H_2O_2$  treated HFFs showed little to no change.

Dox treatment was the only stressor to show a statistically significant decrease in cell body shape index for each concentration tested. The cell body area remained near control levels except for 400 nM, however the perimeter increased significantly for each concentration as well. However, Pal treatment resulted in significant increases in both perimeter and area of the cell body for each concentration, but only a significant decrease in shape index at the highest concentration (20  $\mu$ M). H<sub>2</sub>O<sub>2</sub> treatment induced increased cell body area at and above the concentration of 50  $\mu$ M.

The nuclei showed more significant morphological changes as compared to the cell body. Over all three treatments, there was the general trend of increasing perimeter and area, though shape index for H<sub>2</sub>O<sub>2</sub> and Dox remained relatively unchanged. H<sub>2</sub>O<sub>2</sub> and Pal induced the largest changes in nucleus morphology, with Pal treatment inducing statistically significant increases in perimeter, area, and shape index for all concentrations. In particular, the increasing shape index indicates that the nuclei were becoming more circular rather than elongated. The results indicate that depending on what type of stressor to induce cellular senescence or aging is used, the morphologies of the cells and nuclei can vary, with some expressing greater changes in cell body and others in nuclei. Understanding the mechanism behind senescence induction can indicate what senescent morphologies will present.

All three inducers result in significant increases in SA  $\beta$ -Gal expression, indicative of senescence. Cells treated with Pal of the concentration of 2.5  $\mu$ M had a much higher intensity expression level of  $1.50 \pm 0.02$  a.u. relative to the control group, as compared to the relative intensity expression levels at the optimal concentrations of H<sub>2</sub>O<sub>2</sub> (100  $\mu$ M) and Dox (100 nM) of  $1.19 \pm 0.01$  a.u. and  $1.21 \pm 0.01$  a.u., respectively. This could be due to the lysosomal trapping common in Pal, sometimes observed as the formation of vacuoles within the cytoplasm (Llanos et

al., 2019). Pal is a weak acid; as such, at a neutral pH the drug has a permeable membrane, allowing it to enter the cell body, which becomes impermeable at an acidic pH when the drug is protonated (Llanos et al., 2019). Lysosomes have an acidic pH of about 5.0; as such, when Pal comes into contact with a lysosome within the cytoplasm, it gets trapped within (Garcia-Moreno, 2009). This process of lysosomal trapping may imply that Pal can be stored within the cell. Pal can be released upon washing with PBS or drug-free medium, as the neutral pH of these solutions can permeabilize the drug's membrane and release it from within the cytoplasm. However, it can take hours before any notable decrease in Pal fluorescence is measured (Llanos et al., 2019). As such, this function could account for the much higher relative fluorescence intensity observed.

The increase in phalloidin intensity in all three treatments indicates a higher density of filamentous actin (F-actin), the protein that forms the cytoskeleton of the cell, and stress fibers (Cooper, 2000). Dox induced the greatest increase in phalloidin intensity, with all concentrations resulting in relative intensities greater than 2.3 a.u., whereas Pal peaks at  $1.76 \pm 0.02$  a.u. at 5  $\mu\text{M}$  and  $\text{H}_2\text{O}_2$  at  $1.39 \pm 0.01$  a.u. at 200  $\mu\text{M}$ . Dox treatment in cells has been correlated with the upregulation of vimentin, a binding protein pivotal to cytoskeleton organization (Litwiniec et al., 2010). The tail end of vimentin proteins is known to localize near actin networks within cells, and due to the high synergy between F-actin and vimentin, this can lead to higher F-actin polymerization, though the exact molecular pathway is still unclear (Esue et al., 2006). This mixed vimentin/F-actin network has a relatively high equilibrium dissociation constant, indicating that the bonds are unlikely to dissolve into their component parts. These mixed networks have a higher stiffness than actin-only or intermediate filament-only networks, which can explain the appearance of stress fibers with Dox-treated cell groups (Esue et al., 2006).

Pal induced the next largest increase in phalloidin intensity. However, studies differ on Pal's effects on cytoskeleton restructuring; one study even found that Pal treatment caused an increase in F-actin density in one pancreatic cancer cell line, while reducing it in another (Rencuzogulları et al., 2020). Another study showed that Pal correlates to an upregulation of LIM kinase 1 (LIMK1) in human embryonic kidney cells (HEK-293) and adult acute myeloid leukemia cells (AML) (Jensen et al., 2020). LIMK1 suppresses the expression of actin depolymerizing factor/cofilin proteins, which are used to sever actin filaments and depolymerize F-actin while maintaining cell homeostasis (Arber et al., 1998). As a result, the upregulation of LIMK1 leads to F-actin accumulation and stress fiber formation, which would lead to an increase in phalloidin intensity as observed in this study (Villalonga et al., 2023). However, the effects of Pal on fibroblast cytoskeleton organization are not well studied, and it is not clear what molecular interactions are occurring to result in the increased F-actin density observed in this study. Pal's effect on cytoskeleton organization seems to be cell line dependent.

H<sub>2</sub>O<sub>2</sub> has also been well reported as causing an increase in F-actin content, though of the three stressors it caused the lowest increase. Early studies have shown that H<sub>2</sub>O<sub>2</sub> treatment results in an increase of focal adhesion sites by activating MAPK/SAPK2/p38, a protein that phosphorylates HSP27, the actin polymerization heat shock protein (Huot et al., 1998). This in turn results in a higher polymerization of focal adhesion proteins such as paxillin and vinculin; vinculin in particular binds with F-actin to form fibers across the cell body, and a higher presence of vinculin can result in higher F-actin polymerization (Grandy et al., 2023; Tolbert et al., 2013).

The most unexpected result was the increase in DAPI intensity following drug or H<sub>2</sub>O<sub>2</sub> treatment. One of the phenotypes associated with cellular senescence is the formation of senescence associated heterochromatin foci (SAHF). SAHF are heterochromatin aggregates that

form due to heterochromatin proteins that detach from the nuclear membrane and bind with hypoacetylated histones (Zeng et al., 2018). As DAPI binds to single stranded DNA, these heterochromatin aggregates will bind with more dye, and may account for the increased intensity observed. However, DAPI alone may not be sufficient to confirm the presence of SAHF. Oxidative stress-induced DNA damage may not be the reason for the high intensities after H<sub>2</sub>O<sub>2</sub> application. When applied to cells, H<sub>2</sub>O<sub>2</sub> causes protonation that can excite the dye and result in higher DAPI intensities (Żurek-Biesiada et al., 2013). In the case of Dox, however, DNA damage is likely the causing factor. Treatment with Dox to the cells has been known to result in lowered expression of Lamin B1, a protein that provides structure to the nuclear envelope, as well as the dephosphorylation of Retinoblastoma (Rb), a protein that protects against apoptosis (Antonucci et al., 2014; Bientinesi et al., 2022). Dox treatment also induced an increase in  $\gamma$ -H2AX, a marker of DNA double-strand breaks, and macroH2A1, a histone variant component of SAHF, which indicates the increased DAPI intensity may be due to the formation of SAHF or other related DNA damage (Bientinesi et al., 2022). Similarly, Pal induces DNA damage, and by suppressing the expression of RAD51, a DNA repair protein, inhibits DNA repair; this also results in the increased expression of  $\gamma$ -H2AX, and this DNA damage could be resulting in higher DAPI staining intensity (Wang et al., 2021).

Different stressors can lead to various types of senescence-related changes in morphology and protein expression. Even stressors within the same category, such as Dox and Pal, both being cancer therapy agents, can lead to different manifestations of senescence.

### 3.3 2D vs. 3D Microenvironment Results

We compared the morphological properties of the cell and nucleus for each optimized concentration in 2D and 3D environments. Figure 13 shows the bright field, DAPI, SA  $\beta$ -Gal, and phalloidin images for HFFs treated with each optimal concentration in the 3D collagen gel environment.

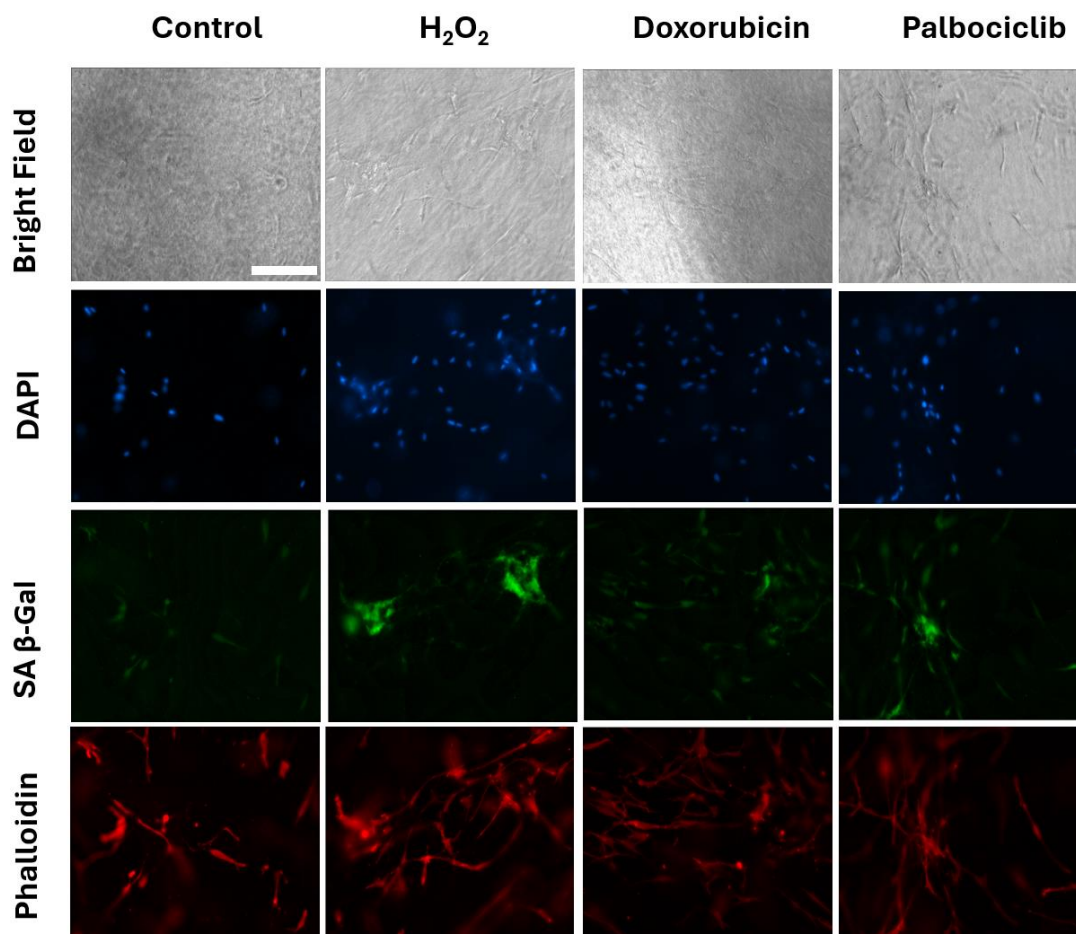


Figure 13: Bright field and immunofluorescence images for HFFs treated with optimal concentrations. Scale bar 200  $\mu$ m.

Figure 14 summarizes morphology results of the nucleus. As expected, it was evident that the nucleus perimeter and area are notably higher on average in 2D environments compared to 3D,



with nearly twice the area in 2D. Cells treated with H<sub>2</sub>O<sub>2</sub> and drugs exhibited a similar trend of change in perimeter and area in both 2D and 3D environments, displaying that the perimeter and area tended to be higher than those of the control group, except for the Dox-treated groups.

The trend of change was shown to be comparable in both environments, with H<sub>2</sub>O<sub>2</sub> and Pal causing increases in perimeter, area, and shape index, while Dox shows little to no increase in perimeter and area, and a decrease in shape index. However, the shape index exhibited greater significance in 3D environments than in 2D, with all three stressors causing statistically significant changes to the nucleus morphology.

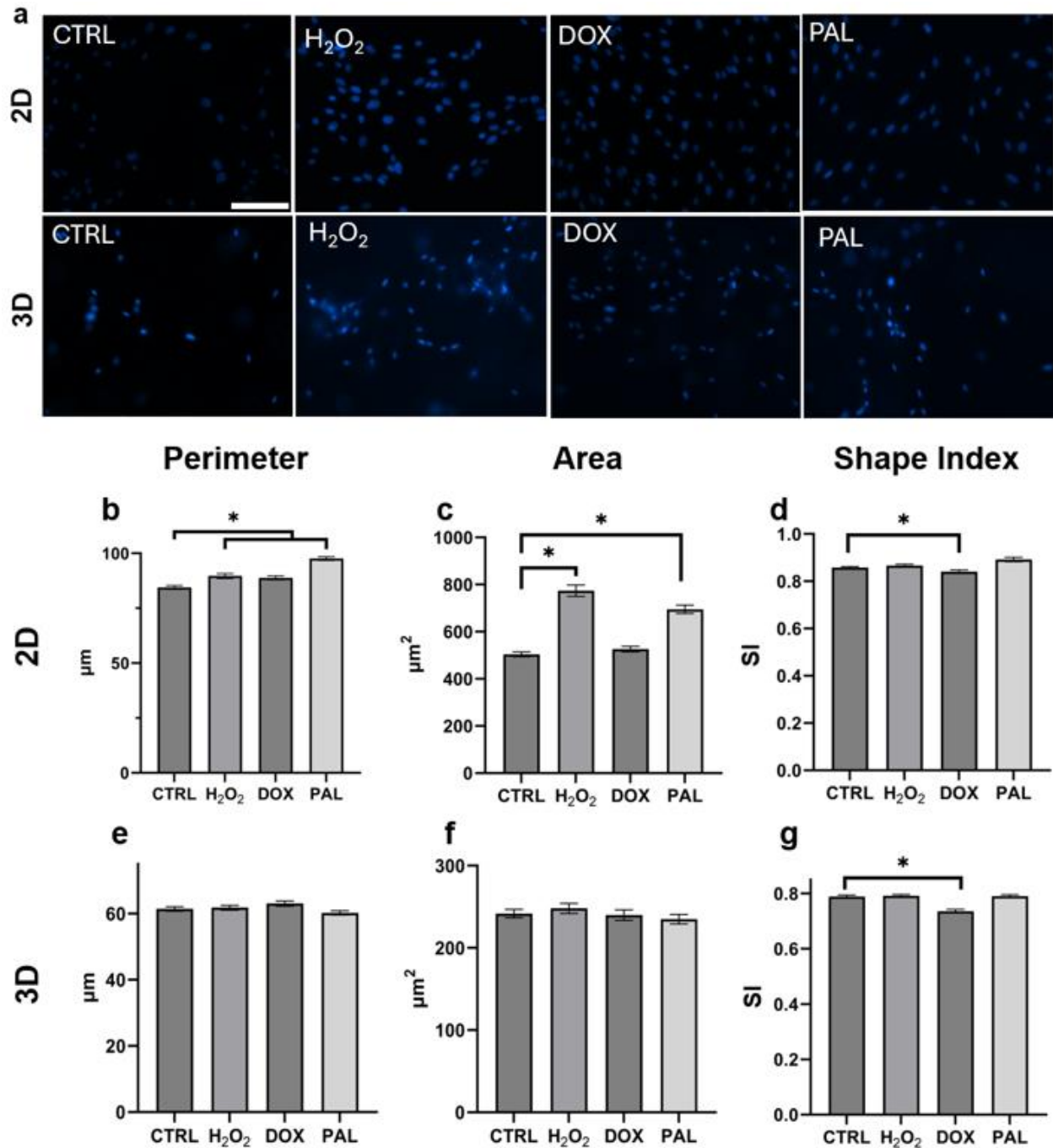


Figure 14: (a) Fluorescence images in nucleus morphology in 2D and 3D. Quantification of nuclear morphological properties for optimized concentrations in (b-d) 2D and (e-g) 3D microenvironments. N = 270, \*  $p \leq 0.05$ . Scale bar 200  $\mu\text{m}$ . Data presented as mean  $\pm$  SEM.

Figure 15 summarizes the quantified morphological properties of cells, based on the fluorescence images of phalloidin, for each optimized concentration in both 2D and 3D

environments. Similar to the results regarding nuclear properties, as anticipated, both the area and perimeter in the 2D environment were approximately two to four times and two times higher, respectively, than those in the 3D environment. When comparing perimeter, in 2D Dox-treated cells displayed significantly higher values ( $393.56 \pm 7.25 \mu\text{m}$ ) than the control group ( $333.6 \pm 18.1 \mu\text{m}$ ), whereas in 3D they displayed significantly lower values ( $298.43 \pm 7.595 \mu\text{m}$ ) than control ( $327.59 \pm 6.999 \mu\text{m}$ ) (Figures 14b, 14e). Pal-treated cells in both 2D and 3D also exhibited higher perimeter values than the control group, although in 3D, the difference was not statistically significant. The  $\text{H}_2\text{O}_2$ -treated group showed no significant change in perimeter in 2D but had a significant decrease ( $304.73 \pm 8.40 \mu\text{m}$ ) compared to control in 3D.

For cellular area in the 2D microenvironment, all treated groups displayed increases as compared to control ( $4214.9 \pm 168.6 \mu\text{m}^2$ ), though only Pal induced a significant increase ( $6728.6 \pm 244.9 \mu\text{m}^2$ ). However, in 3D all treated groups had decreased, with only Dox-treated groups having a statistically significant decrease ( $1307.9 \pm 43.57 \mu\text{m}^2$ ) in comparison to control ( $1686.2 \pm 48.86 \mu\text{m}^2$ ). In 2D, all treated groups had decreases in shape index, with Dox-treated groups inducing a statistically significant decrease ( $0.3771 \pm 0.0079$ ) in comparison to control ( $0.4357 \pm 0.0106$ ). However, in 3D the drug-treated groups remain unchanged, while  $\text{H}_2\text{O}_2$  induced an increase in shape index ( $0.2628 \pm 0.0089$ ) in comparison to control ( $0.2215 \pm 0.0064$ ).

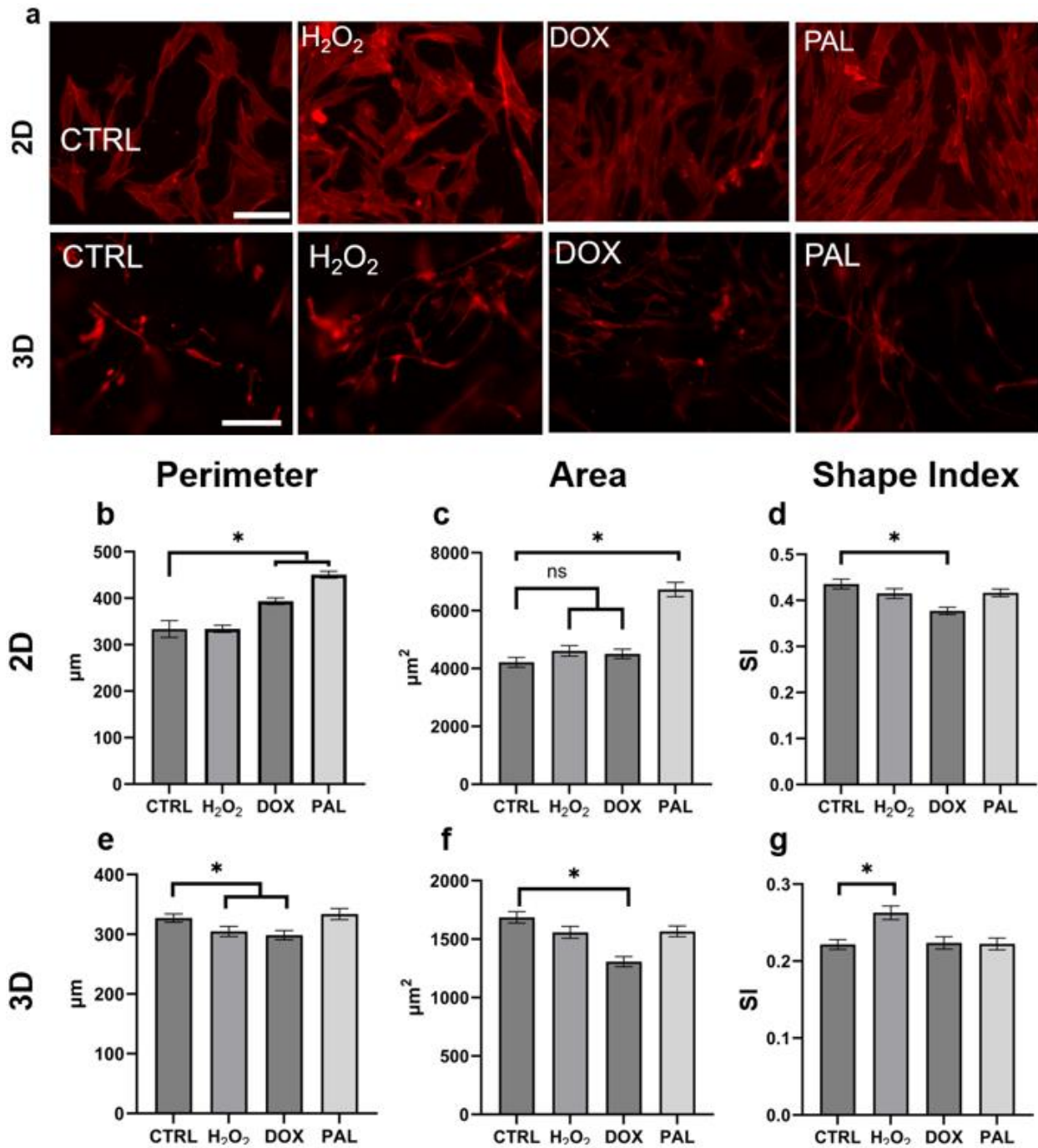


Figure 15: (a) Fluorescence images of phalloidin in 2D and 3D. Quantification of cellular morphological properties for optimized concentrations in (b-d) 2D and (e-g) 3D microenvironments. N = 270, \* p ≤ 0.05. Scale bar 200 μm. Data presented as mean ± SEM.

Figure 16 depicts the quantified results of SA β-Gal activity in HFFs in both 2D and 3D environments. Overall, all three stressors exhibited significant changes in expression in both 2D

and 3D. In 3D, all treated groups experienced at least twofold relative increases in intensity as compared to 3D, whereas in 2D only Pal-treated groups expressed such a large increase.

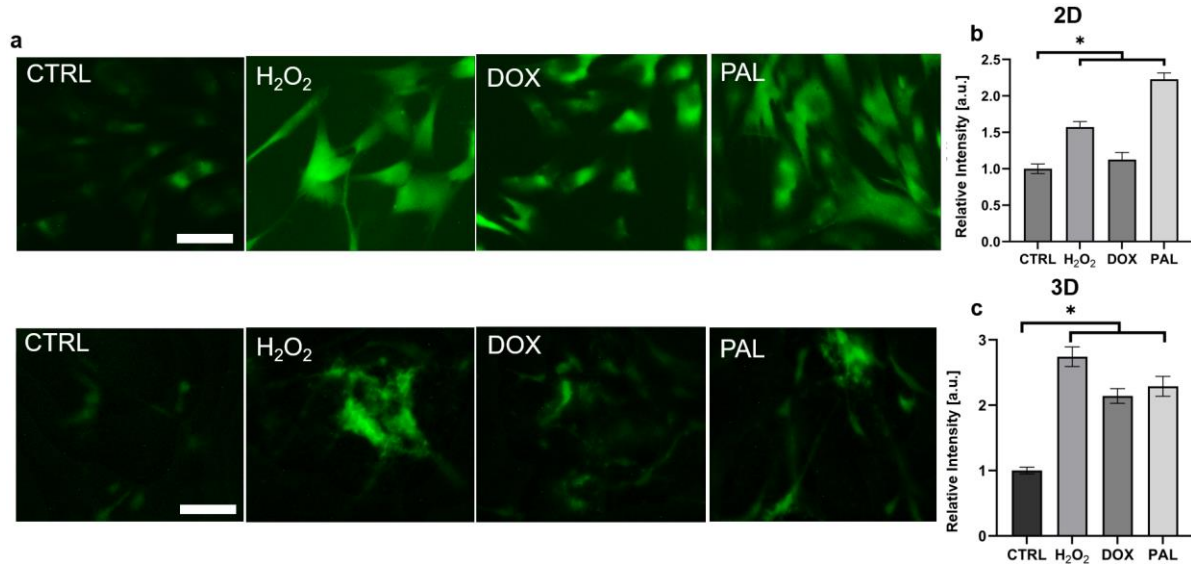


Figure 16: (a) Fluorescence images of SA β-Gal activity in HFFs for each control and each stressor in 2D and 3D environments. Quantified results of the SA β-Gal intensity for (b) 2D and (c) 3D. N = 270, \*  $p \leq 0.05$ . Scale bar 200  $\mu\text{m}$ .

Figure 17 presents the quantified results of phalloidin intensity in both 2D and 3D environments, along with fluorescence images of phalloidin in HFFs for each stressor in both environments. In 2D, all three stressors induced increases in phalloidin fluorescence, with Dox having the highest. However, in 3D, H<sub>2</sub>O<sub>2</sub>- and Dox-treated groups displayed little to no change in comparison to control, and Pal induced a statistically significant decrease.

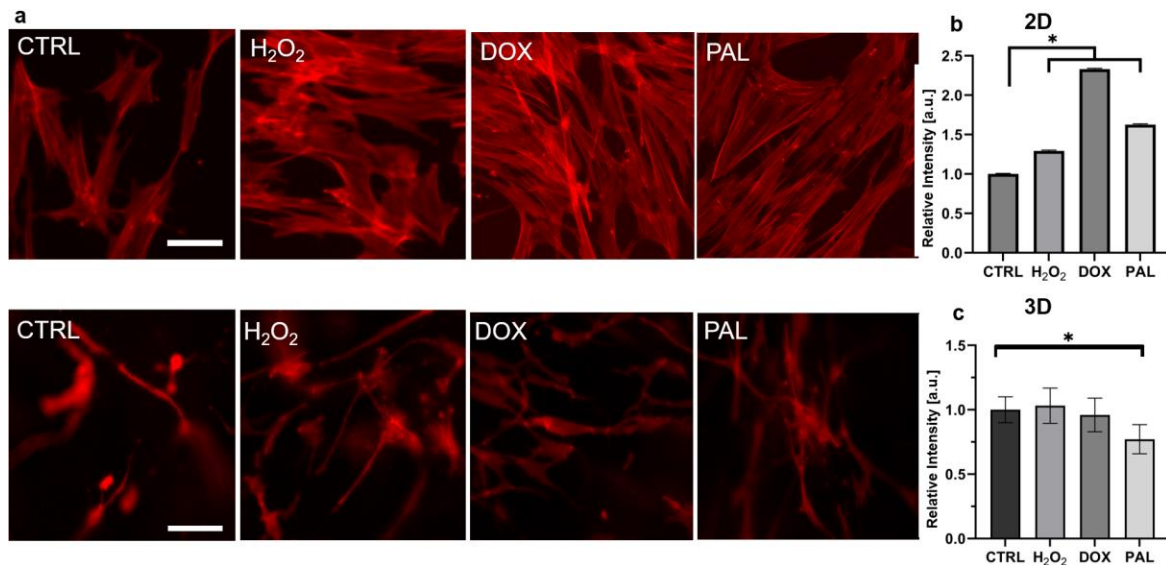


Figure 17: (a) Fluorescence images of phalloidin in HFFs for each control and each stressor in 2D and 3D environments. Quantification of phalloidin intensity for (b) 2D and (c) 3D. N = 270, \*  $p \leq 0.05$ . Data presented as mean  $\pm$  SEM.

Figure 18 illustrates the quantified results of DAPI intensity for both 2D and 3D environments. Overall, all three stressors exhibited significant changes in expression in both 2D and 3D. The increase in fluorescence intensities in 3D is comparable to 2D, except for the Dox-treated group in 3D, which remained near control levels.

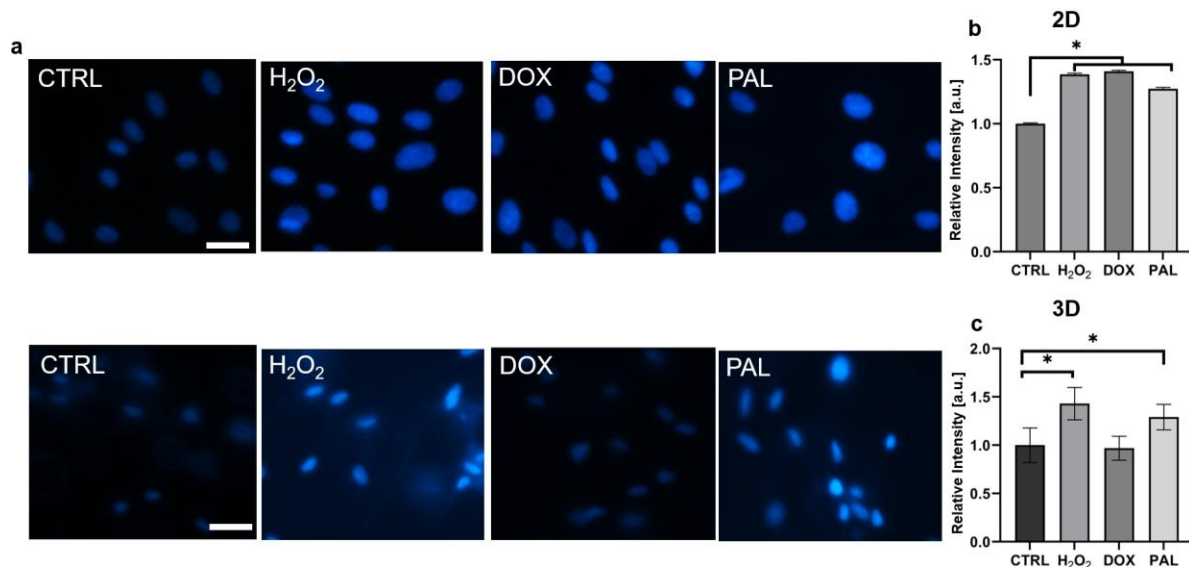


Figure 18: (a) Fluorescence images of DAPI in HFFs for each control and each stressor in 2D and 3D environments. Quantification of DAPI intensity for (b) 2D and (c) 3D. N = 270, \*  $p \leq 0.05$ . Data presented as mean  $\pm$  SEM.

### 3.4 2D vs. 3D Microenvironment Discussion

The expected cell and nucleus enlargement typical of senescence that was observed in the 2D environment was absent in the 3D models. The nuclei remained largely unchanged in size after stressor treatment, and only Dox-treated groups showed a statistically significant decrease in shape index, indicating elongation in 3D. The nuclear enlargement associated with senescence is a result of cell flattening causing the nucleus to flatten as well, rather than changes to the nucleus's functional and morphological properties (Lomakin et al., 2020).

The 3D modelling results indicated no significant enlargement of the cell body. In fact, both H<sub>2</sub>O<sub>2</sub> and Dox caused statistically significant decreases in cell perimeter, and Dox caused statistically significant decrease in cell area. Findings from other 3D models have also indicated that cells do not adopt this 2D senescent morphology, indicating that cell and nucleus enlargement could be an artifact of 2D modeling rather than a senescence related feature (Pauty et al., 2021; Weinmüllner et al., 2020; Yadav et al., 2021). Cells in 3D adopt a more dendritic appearance, with increased elongation even when comparing control cells between environments. Additionally, both the cell body and nucleus less than half the size in area as compared to 2D. The presence of a collagen matrix providing space for growth in all three directions may indicate that changes in volume would be more indicative of size changes induced by senescence.

Pal-treated groups induced twofold increases in SA  $\beta$ -Gal expression in both 2D and 3D relative to control; H<sub>2</sub>O<sub>2</sub> and Dox, however, induced a much higher expression in 3D than compared to 2D. The increase in senescence relative to control for H<sub>2</sub>O<sub>2</sub> and Dox in the 3D environment could be due to the hypoxic nature of the collagen model. It has been observed that 3D environments have a higher accumulation of ROS as compared to 2D (Liu et al., 2018). H<sub>2</sub>O<sub>2</sub> is an ROS, and therefore a form of oxidative stress that induces DNA damage to trigger senescence.

Similarly, Dox produces ROS as well as directly causing DNA damage through the blocking of topoisomerase 2. The lack of sufficient oxygen reaching the cells within the collagen matrix may be contributing to an additional accumulation of ROS, in turn increasing the production of SA  $\beta$ -Gal in the 3D environment.

In the 2D microenvironment, all three stressors resulted in higher phalloidin expression levels relative to control, with Dox-treated groups displaying the largest increase. In the 3D microenvironment, H<sub>2</sub>O<sub>2</sub> and Dox caused no statistically significant change, though H<sub>2</sub>O<sub>2</sub>-treated groups displayed a slight increase and Dox-treated groups a slight decrease. It's important to note that Dox possesses natural red autofluorescence, which could have potentially exacerbated the intensity caused by F-actin restructuring during the quantification of 2D data (Böckelmann et al., 2020). Pal induced a statistically significant decrease, in direct opposition to its effect in 2D. This indicates that Pal's effect on cytoskeletal reorganization is not only cell line dependent, as previously discussed, but also environment dependent. -actin density could be increased post stressor treatment in 2D environments as a way to cope with cell enlargement; however, in 3D environments, the presence of the collagen scaffold provides extracellular support that may be preventing the need for increased F-actin polymerization.

H<sub>2</sub>O<sub>2</sub>- and Pal-treated groups displayed increases in DAPI intensity in both 2D and 3D environments. Dox, while inducing the highest fluorescence in 2D, displayed levels similar to control in 3D. Studies have shown that Dox has difficulty permeating collagen matrices, and the presence of collagen reduces the effects of Dox on cells (Druzhkova et al., 2022; Millerot-Serruot et al., 2010). Studies have shown that collagen-binding integrins used to attach cells to the ECM are correlated with chemoresistance, specifically with Dox (Naci et al., 2019). The collagen/ $\alpha$ 2 $\beta$ 1 integrin inhibits the Rac1 gene, which is necessary in the Dox-induced DNA damage pathway.



Naci et al. observed that Rac1 was necessary for Dox-induced DNA damage, and that the presence of the collagen/ $\alpha2\beta1$  integrin, produced by cell-collagen binding, inhibited the DNA damage response by measuring the DNA damage histone  $\gamma$ -H2AX. The decreased DAPI intensity in the 3D microenvironment, as compared to the high DAPI intensity for Dox-treated groups in 2D, indicates that the presence of the collagen matrix is inhibiting the drug's ability to induce the expected DNA damage. As a result, there is a possibility that the expected SAHF are not forming. However, this would need to be confirmed through assays measuring DNA damage related proteins and more in-depth qualitative study.

## CHAPTER 4

### CONCLUSION

Cellular senescence can be induced through various intrinsic and extrinsic factors. Depending on both the stressor type, as well as the environment, cells may present different senescence related changes. Most research studying senescence uses 2D culture modeling. The wealth of literature describing senescence associated morphological and biochemical changes are largely based on results from 2D modeling. In 2D models, cells often grow, become flatter and misshapen. In 3D, however, it was seen that little change after treatment, with some stressors even causing cells to grow smaller in perimeter and area. This in particular indicates that senescence may not cause cell enlargement, and this phenomenon is an artifact of 2D modeling.

The biochemical changes occurring at the cellular level were also found to be environment dependent, as well as stressor dependent. While in the 2D microenvironment, F-actin density, as measured through phalloidin fluorescence, increased irrespective of stressor, in the 3D microenvironment fluorescence remained at control levels for H<sub>2</sub>O<sub>2</sub> and Dox, and decreased significantly for Pal. Similarly, while DAPI fluorescence increased for all three stressors in 2D, indicating DNA damage, in 3D Dox-treated groups showed no change from control levels. The collagen matrix hinders the drug's ability to enter the nucleus and conduct DNA damage, indicating the presence of the ECM can alter how stressors function in comparison to direct cell interactions.

Overall, it can be seen that senescence related phenotypes differ based on stressor type as well as the cellular microenvironment. While this study was able to show the effects of the microenvironment on cellular morphology changes, the measurements are 2D in nature. In future studies, measuring the volume of cells in both 2D and 3D environments may be more indicative of senescence related morphological changes. Similarly, while DAPI was used as an indirect

measure of DNA damage, further studies using DNA damage specific histone markers could confirm the presence and formation of SAHF. In future works, testing other cell lines, both immortalized and primary human cell lines, with different stressors and in different environments can elucidate how senescence presents differently based on cell type as well. Further measuring changes in mechanical properties, through the use of atomic force microscopy (AFM), as well as measuring SASP levels through MALDI, can reveal greater nuances in stressor dependent senescence. Lastly, using 3D holotomography, studying changes at the organelle level will also be vital.

## REFERENCES

- Antonucci, L. A., Egger, J. V., & Krucher, N. A. (2014). Phosphorylation of the Retinoblastoma protein (Rb) on serine-807 is required for association with Bax. *Cell Cycle*, 13(22), 3611–3617. <https://doi.org/10.4161/15384101.2014.964093>
- Arber, S., Barbayannis, F. A., Hanser, H., Schneider, C., Stanyon, C. A., Bernard, O., & Caroni, P. (1998). Regulation of actin dynamics through phosphorylation of cofilin by LIM-kinase. *Nature*, 393(6687), 805–809. <https://doi.org/10.1038/31729>
- Bientinesi, E., Lulli, M., Becatti, M., Ristori, S., Margheri, F., & Monti, D. (2022). Doxorubicin-induced senescence in normal fibroblasts promotes in vitro tumour cell growth and invasiveness: The role of Quercetin in modulating these processes. *Mechanisms of Ageing and Development*, 206, 111689. <https://doi.org/10.1016/j.mad.2022.111689>
- Böckelmann, L., Starzonek, C., Niehoff, A.-C., Karst, U., Thomale, J., Schlüter, H., Bokemeyer, C., Aigner, A., & Schumacher, U. (2020). Detection of doxorubicin, cisplatin and therapeutic antibodies in formalin-fixed paraffin-embedded human cancer cells. *Histochemistry and Cell Biology*, 153(5), 367–377. <https://doi.org/10.1007/s00418-020-01857-x>
- Cooper, G. (2000). Structure and Organization of Actin Filaments. In *The Cell: A Molecular Approach* (2nd ed.). Sinauer Associates.
- Coppé, J.-P., Desprez, P.-Y., Krtolica, A., & Campisi, J. (2010). The Senescence-Associated Secretory Phenotype: The Dark Side of Tumor Suppression. *Annual Review of Pathology: Mechanisms of Disease*, 5(1), 99–118. <https://doi.org/10.1146/annurev-pathol-121808-102144>

- Csekes, E., & Račková, L. (2021). Skin Aging, Cellular Senescence and Natural Polyphenols. *International Journal of Molecular Sciences*, 22(23), 12641.  
<https://doi.org/10.3390/ijms222312641>
- de Mera-Rodríguez, J. A., Álvarez-Hernán, G., Gañán, Y., Martín-Partido, G., Rodríguez-León, J., & Francisco-Morcillo, J. (2021). Is Senescence-Associated  $\beta$ -Galactosidase a Reliable in vivo Marker of Cellular Senescence During Embryonic Development? *Frontiers in Cell and Developmental Biology*, 9. <https://doi.org/10.3389/fcell.2021.623175>
- Druzhkova, I., Nikonova, E., Ignatova, N., Koryakina, I., Zyuzin, M., Mozherov, A., Kozlov, D., Krylov, D., Kuznetsova, D., Lisitsa, U., Shcheslavskiy, V., Shirshin, E. A., Zagaynova, E., & Shirmanova, M. (2022). Effect of Collagen Matrix on Doxorubicin Distribution and Cancer Cells' Response to Treatment in 3D Tumor Model. *Cancers*, 14(22), 5487.  
<https://doi.org/10.3390/cancers14225487>
- Duan, J., Duan, J., Zhang, Z., & Tong, T. (2005). Irreversible cellular senescence induced by prolonged exposure to H<sub>2</sub>O<sub>2</sub> involves DNA-damage-and-repair genes and telomere shortening. *The International Journal of Biochemistry & Cell Biology*, 37(7), 1407–1420.  
<https://doi.org/10.1016/j.biocel.2005.01.010>
- Esue, O., Carson, A. A., Tseng, Y., & Wirtz, D. (2006). A Direct Interaction between Actin and Vimentin Filaments Mediated by the Tail Domain of Vimentin. *Journal of Biological Chemistry*, 281(41), 30393–30399. <https://doi.org/10.1074/jbc.M605452200>
- Ewald, J. A., Desotelle, J. A., Wilding, G., & Jarrard, D. F. (2010). Therapy-Induced Senescence in Cancer. *JNCI: Journal of the National Cancer Institute*, 102(20), 1536–1546.  
<https://doi.org/10.1093/jnci/djq364>

- Fitsiou, E., Pulido, T., Campisi, J., Alimirah, F., & Demaria, M. (2021). Cellular Senescence and the Senescence-Associated Secretory Phenotype as Drivers of Skin Photoaging. *Journal of Investigative Dermatology*, 141(4), 1119–1126. <https://doi.org/10.1016/j.jid.2020.09.031>
- Freund, A., Laberge, R.-M., Demaria, M., & Campisi, J. (2012). Lamin B1 loss is a senescence-associated biomarker. *Molecular Biology of the Cell*, 23(11), 2066–2075. <https://doi.org/10.1091/mbc.e11-10-0884>
- Garbacki, N., Willems, J., Neutelings, T., Lambert, C., Deroanne, C., Adrian, A., Franz, M., Maurer, M., De Gieter, P., Nusgens, B., & Colige, A. (2023). Microgravity triggers ferroptosis and accelerates senescence in the MG-63 cell model of osteoblastic cells. *Npj Microgravity*, 9(1), 91. <https://doi.org/10.1038/s41526-023-00339-3>
- Garcia-Moreno, B. (2009). Adaptations of proteins to cellular and subcellular pH. *Journal of Biology*, 8(11), 98. <https://doi.org/10.1186/jbiol199>
- Gerasymchuk, M., Robinson, G. I., Kovalchuk, O., & Kovalchuk, I. (2022). Modeling of the Senescence-Associated Phenotype in Human Skin Fibroblasts. *International Journal of Molecular Sciences*, 23(13). <https://doi.org/10.3390/ijms23137124>
- Gordon, R. R., & Nelson, P. S. (2012). Cellular senescence and cancer chemotherapy resistance. *Drug Resistance Updates*, 15(1–2), 123–131. <https://doi.org/10.1016/j.drug.2012.01.002>
- Grandy, C., Port, F., Radzinski, M., Singh, K., Erz, D., Pfeil, J., Reichmann, D., & Gottschalk, K.-E. (2023). Remodeling of the focal adhesion complex by hydrogen-peroxide-induced senescence. *Scientific Reports*, 13(1), 9735. <https://doi.org/10.1038/s41598-023-36347-2>
- Huang, W., Hickson, L. J., Eirin, A., Kirkland, J. L., & Lerman, L. O. (2022). Cellular senescence: the good, the bad and the unknown. *Nature Reviews Nephrology*, 18(10), 611–627. <https://doi.org/10.1038/s41581-022-00601-z>

- Huot, J., Houle, F., Rousseau, S., Deschesnes, R. G., Shah, G. M., & Landry, J. (1998). SAPK2/p38-dependent F-Actin Reorganization Regulates Early Membrane Blebbing during Stress-induced Apoptosis. *The Journal of Cell Biology*, *143*(5), 1361–1373. <https://doi.org/10.1083/jcb.143.5.1361>
- Jensen, P., Carlet, M., Schlenk, R. F., Weber, A., Kress, J., Brunner, I., Słabicki, M., Grill, G., Weisemann, S., Cheng, Y.-Y., Jeremias, I., Scholl, C., & Fröhling, S. (2020). Requirement for LIM kinases in acute myeloid leukemia. *Leukemia*, *34*(12), 3173–3185. <https://doi.org/10.1038/s41375-020-0943-5>
- Johnson-Arbor, K., & Dubey, R. (2024, January). *Doxorubicin*. StatPearls Publishing.
- Kuilman, T., Michaloglou, C., Mooi, W. J., & Peeper, D. S. (2010). The essence of senescence. *Genes & Development*, *24*(22), 2463–2479. <https://doi.org/10.1101/gad.1971610>
- Lahalle, A., Lacroix, M., De Blasio, C., Cissé, M. Y., Linares, L. K., & Le Cam, L. (2021). The p53 Pathway and Metabolism: The Tree That Hides the Forest. *Cancers*, *13*(1), 133. <https://doi.org/10.3390/cancers13010133>
- Litwiniec, A., Grzanka, A., Helmin-Basa, A., Gackowska, L., & Grzanka, D. (2010). Features of senescence and cell death induced by doxorubicin in A549 cells: organization and level of selected cytoskeletal proteins. *Journal of Cancer Research and Clinical Oncology*, *136*(5), 717–736. <https://doi.org/10.1007/s00432-009-0711-4>
- Liu, Q., Zhang, Z., Liu, Y., Cui, Z., Zhang, T., Li, Z., & Ma, W. (2018). Cancer cells growing on perfused 3D collagen model produced higher reactive oxygen species level and were more resistant to cisplatin compared to the 2D model. *Journal of Applied Biomaterials & Functional Materials*, *16*(3), 144–150. <https://doi.org/10.1177/2280800018764763>

- Llanos, S., Megias, D., Blanco-Aparicio, C., Hernández-Encinas, E., Rovira, M., Pietrocola, F., & Serrano, M. (2019). Lysosomal trapping of palbociclib and its functional implications. *Oncogene*, 38(20), 3886–3902. <https://doi.org/10.1038/s41388-019-0695-8>
- Lomakin, A. J., Cattin, C. J., Cuvelier, D., Alraies, Z., Molina, M., Nader, G. P. F., Srivastava, N., Sáez, P. J., Garcia-Arcos, J. M., Zhitnyak, I. Y., Bhargava, A., Driscoll, M. K., Welf, E. S., Fiolka, R., Petrie, R. J., De Silva, N. S., González-Granado, J. M., Manel, N., Lennon-Duménil, A. M., ... Piel, M. (2020). The nucleus acts as a ruler tailoring cell responses to spatial constraints. *Science*, 370(6514). <https://doi.org/10.1126/science.aba2894>
- Low, E., Alimohammadiha, G., Smith, L. A., Costello, L. F., Przyborski, S. A., von Zglinicki, T., & Miwa, S. (2021a). How good is the evidence that cellular senescence causes skin ageing? *Ageing Research Reviews*, 71, 101456. <https://doi.org/10.1016/j.arr.2021.101456>
- Low, E., Alimohammadiha, G., Smith, L. A., Costello, L. F., Przyborski, S. A., von Zglinicki, T., & Miwa, S. (2021b). How good is the evidence that cellular senescence causes skin ageing? *Ageing Research Reviews*, 71, 101456. <https://doi.org/10.1016/j.arr.2021.101456>
- Millerot-Serruot, E., Guilbert, M., Fourré, N., Witkowski, W., Said, G., Van Gulick, L., Terryn, C., Zahm, J.-M., Garnotel, R., & Jeannesson, P. (2010). 3D collagen type I matrix inhibits the antimigratory effect of doxorubicin. *Cancer Cell International*, 10(1), 26. <https://doi.org/10.1186/1475-2867-10-26>
- Milligan, D. A., Tyler, E. J., & Bishop, C. L. (2020). Tissue engineering to better understand senescence: Organotypics come of age. *Mechanisms of Ageing and Development*, 190, 111261. <https://doi.org/10.1016/j.mad.2020.111261>
- Muñoz-Espín, D., & Serrano, M. (2014). Cellular senescence: from physiology to pathology. *Nature Reviews Molecular Cell Biology*, 15(7), 482–496. <https://doi.org/10.1038/nrm3823>



- Naci, D., Berrazouane, S., Barabé, F., & Aoudjit, F. (2019). Cell adhesion to collagen promotes leukemia resistance to doxorubicin by reducing DNA damage through the inhibition of Rac1 activation. *Scientific Reports*, 9(1), 19455. <https://doi.org/10.1038/s41598-019-55934-w>
- Narita, M., Nuñez, S., Heard, E., Narita, M., Lin, A. W., Hearn, S. A., Spector, D. L., Hannon, G. J., & Lowe, S. W. (2003). Rb-Mediated Heterochromatin Formation and Silencing of E2F Target Genes during Cellular Senescence. *Cell*, 113(6), 703–716. [https://doi.org/10.1016/S0092-8674\(03\)00401-X](https://doi.org/10.1016/S0092-8674(03)00401-X)
- Pauty, J., Nakano, S., Usuba, R., Nakajima, T., Johmura, Y., Omori, S., Sakamoto, N., Kikuchi, A., Nakanishi, M., & Matsunaga, Y. T. (2021). A 3D tissue model-on-a-chip for studying the effects of human senescent fibroblasts on blood vessels. *Biomaterials Science*, 9(1), 199–211. <https://doi.org/10.1039/D0BM01297A>
- Phillip, J. M., Aifuwa, I., Walston, J., & Wirtz, D. (2015). The Mechanobiology of Aging. *Annual Review of Biomedical Engineering*, 17(1), 113–141. <https://doi.org/10.1146/annurev-bioeng-071114-040829>
- Rencuzogulları, O., Yerlikaya, P. O., Gürkan, A. Ç., Arisan, E. D., & Telci, D. (2020). Palbociclib, a selective CDK4/6 inhibitor, restricts cell survival and epithelial-mesenchymal transition in Panc-1 and MiaPaCa-2 pancreatic cancer cells. *Journal of Cellular Biochemistry*, 121(1), 508–523. <https://doi.org/10.1002/jcb.29249>
- Saqib, S., Akram, A., Halim, S. A., & Tassaduq, R. (2017). Sources of  $\beta$ -galactosidase and its applications in food industry. *3 Biotech*, 7(1), 79. <https://doi.org/10.1007/s13205-017-0645-5>

- Schmitt, R., & Melk, A. (2022). Characteristics of senescent cells. In *Regenerative Nephrology* (pp. 231–240). Elsevier. <https://doi.org/10.1016/B978-0-12-823318-4.00035-4>
- Siegel, R. L., Giaquinto, A. N., & Jemal, A. (2024). Cancer statistics, 2024. *CA: A Cancer Journal for Clinicians*, 74(1), 12–49. <https://doi.org/10.3322/caac.21820>
- Snezhkina, A. V., Kudryavtseva, A. V., Kardymon, O. L., Savvateeva, M. V., Melnikova, N. V., Krasnov, G. S., & Dmitriev, A. A. (2019). ROS Generation and Antioxidant Defense Systems in Normal and Malignant Cells. *Oxidative Medicine and Cellular Longevity*, 2019, 1–17. <https://doi.org/10.1155/2019/6175804>
- Tolbert, C. E., Burridge, K., & Campbell, S. L. (2013). Vinculin regulation of F-actin bundle formation. *Cell Adhesion & Migration*, 7(2), 219–225. <https://doi.org/10.4161/cam.23184>
- Torrens-Mas, M., Perelló-Reus, C., Navas-Enamorado, C., Ibargüen-González, L., Sanchez-Polo, A., Segura-Sampedro, J. J., Masmiquel, L., Barcelo, C., & Gonzalez-Freire, M. (2021). Organoids: An Emerging Tool to Study Aging Signature across Human Tissues. Modeling Aging with Patient-Derived Organoids. *International Journal of Molecular Sciences*, 22(19), 10547. <https://doi.org/10.3390/ijms221910547>
- Toussaint, O., Medrano, E. E., & von Zglinicki, T. (2000). Cellular and molecular mechanisms of stress-induced premature senescence (SIPS) of human diploid fibroblasts and melanocytes. *Experimental Gerontology*, 35(8), 927–945. [https://doi.org/10.1016/S0531-5565\(00\)00180-7](https://doi.org/10.1016/S0531-5565(00)00180-7)
- Toussaint, O., Royer, V., Salmon, M., & Remacle, J. (2002). Stress-induced premature senescence and tissue ageing. *Biochemical Pharmacology*, 64(5–6), 1007–1009. [https://doi.org/10.1016/S0006-2952\(02\)01170-X](https://doi.org/10.1016/S0006-2952(02)01170-X)

- Tworowski, E., Glucksberg, M. R., & Johnson, M. (2018). The effect of the rate of hydrostatic pressure depressurization on cells in culture. *PLOS ONE*, *13*(1), e0189890.  
<https://doi.org/10.1371/journal.pone.0189890>
- Valieva, Y., Ivanova, E., Fayzullin, A., Kurkov, A., & Igrunkova, A. (2022). Senescence-Associated  $\beta$ -Galactosidase Detection in Pathology. *Diagnostics*, *12*(10), 2309.  
<https://doi.org/10.3390/diagnostics12102309>
- Villalonga, E., Mosrin, C., Normand, T., Girardin, C., Serrano, A., Žunar, B., Doudeau, M., Godin, F., Bénédicti, H., & Vallée, B. (2023). LIM Kinases, LIMK1 and LIMK2, Are Crucial Node Actors of the Cell Fate: Molecular to Pathological Features. *Cells*, *12*(5), 805.  
<https://doi.org/10.3390/cells12050805>
- Wagner, V., & Gil, J. (2020). Senescence as a therapeutically relevant response to CDK4/6 inhibitors. *Oncogene*, *39*(29), 5165–5176. <https://doi.org/10.1038/s41388-020-1354-9>
- Wang, T.-H., Chen, C.-C., Leu, Y.-L., Lee, Y.-S., Lian, J.-H., Hsieh, H.-L., & Chen, C.-Y. (2021). Palbociclib induces DNA damage and inhibits DNA repair to induce cellular senescence and apoptosis in oral squamous cell carcinoma. *Journal of the Formosan Medical Association*, *120*(9), 1695–1705. <https://doi.org/10.1016/j.jfma.2020.12.009>
- Weinmüller, R., Zbiral, B., Becirovic, A., Stelzer, E. M., Nagelreiter, F., Schosserer, M., Lämmermann, I., Liendl, L., Lang, M., Terlecki-Zaniewicz, L., Andriotis, O., Mildner, M., Golabi, B., Waidhofer-Söllner, P., Schedle, K., Emsenhuber, G., Thurner, P. J., Tschachler, E., Gruber, F., & Grillari, J. (2020). Organotypic human skin culture models constructed with senescent fibroblasts show hallmarks of skin aging. *Npj Aging and Mechanisms of Disease*, *6*(1), 4. <https://doi.org/10.1038/s41514-020-0042-x>

- Xiao, S., Qin, D., Hou, X., Tian, L., Yu, Y., Zhang, R., Lyu, H., Guo, D., Chen, X.-Z., Zhou, C., & Tang, J. (2023). Cellular senescence: a double-edged sword in cancer therapy. *Frontiers in Oncology*, 13. <https://doi.org/10.3389/fonc.2023.1189015>
- Yadav, P., Chatterjee, K., & Saini, D. K. (2021). Senescent cells in 3D culture show suppressed senescence signatures. *Biomaterials Science*, 9(19), 6461–6473. <https://doi.org/10.1039/D1BM00536G>
- Young, A. R. J., Narita, M., Ferreira, M., Kirschner, K., Sadaie, M., Darot, J. F. J., Tavaré, S., Arakawa, S., Shimizu, S., Watt, F. M., & Narita, M. (2009). Autophagy mediates the mitotic senescence transition. *Genes & Development*, 23(7), 798–803. <https://doi.org/10.1101/gad.519709>
- Zeng, S., Shen, W., & Liu, L. (2018). Senescence and Cancer. *Cancer Translational Medicine*, 4(3), 70. [https://doi.org/10.4103/ctm.ctm\\_22\\_18](https://doi.org/10.4103/ctm.ctm_22_18)
- Żurek-Biesiada, D., Kędracka-Krok, S., & Dobrucki, J. W. (2013). UV-activated conversion of Hoechst 33258, DAPI, and Vybrant DyeCycle fluorescent dyes into blue-excited, green-emitting protonated forms. *Cytometry Part A*, 83A(5), 441–451. <https://doi.org/10.1002/cyto.a.22260>

## CURRICULUM VITAE

Apoorva Chauhan

Email: apoorvasc123@gmail.com

### EDUCATION

University of Nevada Las Vegas, Honors College, Las Vegas, NV 2018-2022

*Bachelor of Science in Mechanical Engineering, magna cum laude*

*Bachelor of Science in Business Administration/Management, magna cum laude*

University of Nevada Las Vegas, Las Vegas, NV

2022-2024

*Master of Science in Biomedical Engineering*

*Relevant courses included:*

- Mechanobiology
- Stem Cell Regenerative Biology
- Introduction to Biomedical Devices
- Biomechanical Applications in Kinesiology
- Transportation Phenomena in Bioengineering

### EXPERIENCE

*Mechanobiology Lab* – UNLV, Las Vegas, NV

Graduate Researcher, January 2023 to May 2024

Lab manager leading research on induced aging in human skin tissue

- Developing new methods to measure aging in 3D physiologically relevant environments
- Investigating new biomarkers of aging to develop robust disease models and therapies

*Everi Holdings Inc.* – Las Vegas, NV

Operations Intern, September 2020 to September 2023

Las Vegas based company that produces gaming, financial, and loyalty machines

- Communicate with clients to access remote servers to migrate data to new database system
- Leverage internal systems to update customer requested fee changes and create merchant files on a product server to enable modular functionality at specific properties

*U.S. Dept. of Energy 2020 Solar Decathlon - Team Las Vegas* – UNLV, Las Vegas, NV

Energy Team Lead, 2019 to 2021

International, collegiate competition to design, build, and operate a full-scale, net-zero energy home.

- Optimized building design with 60% energy load reduction using energy modeling software Building Energy Optimization Tool (BEopt) and home energy analysis REM/Rate.
- Won 3<sup>rd</sup> place international

*Diabetic Neuropathy Machine Learning Research* – UNLV, Las Vegas, NV

Undergraduate Researcher, 2019 to 2023

- Published article analyzing pressure data from 109 participants to develop new diagnosis process for diabetic neuropathy
- Analyzed data in MATLAB to assess 33 machine learning algorithms used for diagnosis
- Directed and engaged with participants during data collection process

*National Summer Transportation Institute* – UNLV, Las Vegas, NV

Program Assistant, Summer 2019

UNLV summer STEM camp for low-income, minority high school students.

- Organized over 35 sponsors to provide lectures, field trips, housing, and food for 25 high school students.
- Created and managed schedules, presentations, and financial materials for funding and day-to-day operation

## PUBLICATIONS

### Peer Review Journal Articles

**Chauhan, A. S.**, Varre, M. S., Izuora, K., Trabia, M. B., & Dufek, J. S. (2023). Prediction of Diabetes Mellitus Progression Using Supervised Machine Learning. *Sensors* (Basel, Switzerland), 23(10), 4658. <https://doi.org/10.3390/s23104658>

### Poster Presentation

**Chauhan, A.S.** (2023, October 11-14). Characterizing functional properties of hydrogen peroxide-induced cellular senescence [Poster presentation]. 2023 BMES Annual Meeting, Seattle, WA, USA.

**Chauhan, A.S.** (2022, June 22-23). Prediction of Diabetes Mellitus used supervised machine learning [Poster presentation]. 2022 Summer Biomechanics, Bioengineering, and Biotransport Conference, Cambridge, MD, USA.

## SKILLS

- Professional fluency in Hindi and Spanish
- Experienced in MATLAB, SolidWorks, and Python
- OSHA 10 certified

## HONORS AND AWARDS

GPSA Sponsorship Award	2023
Office of Undergraduate Research Travel Award	2022
Dean's List for 8 semesters, University of Nevada Las Vegas	2018-2022
Federal SEOG Grant	2021
Bob Davis Scholarship	2021
President's Scholarship, University of Nevada Las Vegas	2018-2022
Federal Pell Grant	2018-2022
National Merit Scholarship Finalist	2018-2022
Millenium Scholarship	2018-2022